Review — Magnetism, magnetic materials, and interdisciplinary research

Development and application of ferrite materials for low temperature co-fired ceramic technology*

Zhang Huai-Wu(张怀武)†, Li Jie(李 颉), Su Hua(苏 桦)‡,
Zhou Ting-Chuan(周廷川), Long Yang(龙 洋), and Zheng Zong-Liang(郑宗良)

State Key Laboratory of Electronic Thin Films and Integrated Devices, University of Electronic Science and Technology of China, Chengdu 610054, *China*

(Received 9 August 2013)

Development and application of ferrite materials for low temperature co-fired ceramic (LTCC) technology are discussed, specifically addressing several typical ferrite materials such as M-type barium ferrite, NiCuZn ferrite, YIG ferrite, and lithium ferrite. In order to permit co-firing with a silver internal electrode in LTCC process, the sintering temperature of ferrite materials should be less than 950 °C. These ferrite materials are research focuses and are applied in many ways in electronics.

Keywords: ferrite materials, low temperature co-fired ceramic technology

PACS: 75.75.–c, 75.50.–y, 75.70.Cn **DOI:** 10.1088/1674-1056/22/11/117504

1. Introduction

Ever since Neolithic man first used a piece of suspended lodestone to navigate, mankind has used magnetic materials of various kinds. However, it was not until the advent of electricity that the magnetic processes began to be understood. It is now known that lodestone is an iron ore, magnetite, which is one of a wide range of magnetic ceramics based on iron (III) oxide, called ferrites. Magnetite, Fe_3O_4 is in a structural class of compounds known as the spinels with the composition $MeFe_2O_4$, where Me is a divalent cation, Fe^{2+} in the case of magnetite. With the development of industrial electronics, magnetic materials were used in a multitude of applications, for example motors, generators, transformers, actuators, antennas, and sensors, information storage, mobile communications, transport, security, defense, and aerospace, diagnostic devices and a means to focus electron beams.

Since barium hexaferrite was originally examined in the late 1930s by Adelskold, and further studied by Gorter and Braun at Philips in the 1950s, the unique properties associated with its anisotropic magnetic and crystalline structures have made the system of great interest to both scientists and engineers.[1] Barium ferrites have a magnetoplumbite structures, with space group P_3^6/mmc. The crystal structure of barium ferrite can be described as a stacking sequence of the basic blocks RSR*S* where the R contains a two O_4-layer block and one BaO_3 with the composition ($Ba^{2+}Fe_6^{3+}O_{11}^{2-}$), and S is a block with two O_4-layer with the composition $Fe_6^{3+}O_8^{2-}$. The asterisk means that the corresponding block is turned 180° around the *c* axis.[2] These ferrites have become massively important materials commercially and technologically, accounting for the bulk of the total magnetic materials manufactured globally, and they have a multitude of uses and applications. As well as their use as permanent magnets, common applications are as magnetic recording and data storage materials, and as components in electrical devices, particularly those operating at microwave/GHz frequencies.[3]

Traditional spinel NiZn (including NiCuZn) ferrites are widely used in various high-frequency components and multilayer chip inductors (MLCI) due to their high electrical resistivity, chemical stability, relatively low sintering temperature, and good electromagnetic properties. However, in power field applications, such as switch-mode power supplies (SMPS), MnZn power ferrites are dominant because of their high saturation flux density (B_s) and low power loss (P_{cv}) characteristics. Recently, the rising frequency of SMPS and further miniaturization of magnetic components enable the use of NiZn ferrites, because they have high electrical resistivity and can miniaturize magnetic components without a bobbin. Second, permeability spectra of NiCuZn ferrites with different microstructures were resolved into contributions of domain wall resonance and spin rotation relaxation. The fitting results of the permeability dispersion revealed the relationships among domain wall resonance, spin rotation relaxation mechanisms and microstructures. It was found that when the ferrite was excited under large flux density, the sample with larger average grain size and closed pores could obtain lower P_{cv}. However,

*Project supported by the National Basic Research Program of China (Grant No. 2012CB933100), the National Natural Science Foundation of China (Grant Nos. 51132003, 61021061, and 61171047), and the Second Item of Strongpoint Industry of Guangdong Province, China (Grant No. 2012A090100001).

†Corresponding author. E-mail: hwzhang@uestc.edu.cn

‡Corresponding author. E-mail: uestcsh@163.com

© 2013 Chinese Physical Society and IOP Publishing Ltd

for the low induction condition, the ferrite with small grain size had better performance on P_{cv}.

With the development of integrated devices in radio frequency (RF), microwave/millimeter-wave, terahertz wave, and optical band, is the question arises: how can we investigate a kind of film in microwave, terahertz (THz), and optical devices and realize the integrated devices in a range from microwave to optical band.[4–7] In recent years, all kinds of garnet films were designed based on its low propagating loss in microwave devices and magneto-optical devices and potential application in terahertz band.[8] For magneto-optical application need liquid phase epitaxy (LPE) materials such as Bi:YIG, Ce:YIG, Bi:LuIG to act as the deflector, switch,[9] modulator, isolator, circulator, rotator, and sensors,[10–14] need RF magnetron sputtering polycrystalline film Bi:DyIG as magneto-optical recording application.[12–14] In microwave /millimeter-wave application fields, single-or polycrystalline garnet films thickness from 0.2 μm to 100 μm were necessary to gyro magnetic devices filter, delay line, isolator, and limiter,[11–15] also single-crystal garnet films for magneto-static surface wave (MSSW) devices such as modulator, filter, delay, transpose, etc. In THz applications fields, single- or polycrystalline films were used to the artificial crystal THz waveguide, filter, switch, modulator, isolator, circulator, etc, by liquid phase epitaxy,[18–23] the crystal structure of garnet YIG, Bi:LuIG or Bi:YIG thin film growth on 3-inch GGG single crystal and along the (111) crystal plane is shown in Fig. 1.

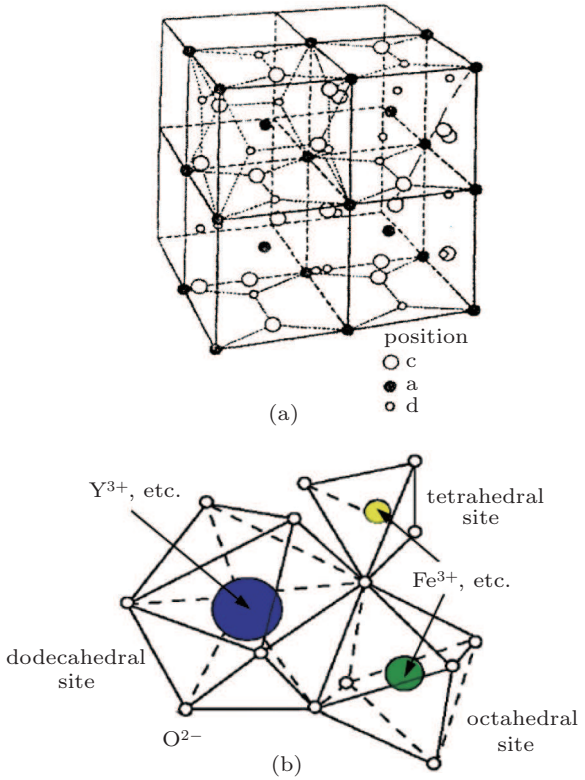


Fig. 1. Garnet crystal structure. (a) Lattice structure and (b) interstitial site.

The general formula $\{C_3\}$ $[A_2](D_3)O_{12}$, where tabs { }, [ ], and ( ) describe cations occupying dodecahedral sites, octahedral sites, and tetrahedral sites, and the unit cell consists of 160 atoms or 8 formula units. According to today's requirements for microwave devices, broad band and integrated devices must possession perfect single-crystal film structures, small ferromagnetic resonance (FMR) ΔH, a smooth surface and low defect density, large size (3–4 inch) homogenous films and lead free growth technique. For magneto-optical devices, excellent single-crystal or polycrystal film structures must be grown, and films must possess a smooth surface and low defect density, large Farady angle, 3–4 inch homogenous films, and flexibility must be allowed in the selection of substrate.[24–28]

Lithium ferrites with their unique advantages are concerned by many scholars. As early as 1960's and 1970's, many scholars launched studies of lithium ferrites, but most studies focused on the ferrite materials used below the X-band frequency. Many researchers studied the problem that sintering lithium ferrites at high temperature leads to evaporation of Li_2O and emergence of Fe^{2+} ions. In 1969, Pointon *et al.* studied solid state reactions in lithium ferrite, the low-temperature decomposition of lithium carbonate in an intimate mixture with hematite (α-Fe_2O_3), the volatilization of lithia at high sintering temperatures, and the retardation of the sintering reaction by applied oxygen pressure.[29] The study showed that lithium carbonate decomposes at about 400 °C and takes part in solid state reactions with hematite, the decomposition reaction in this case is

$$Li_2CO_3 + Fe_2O_3 \rightarrow 2LiFeO_2 + CO_2\uparrow. \quad (1)$$

In the subsequent sintering process, $2LiFeO_2$ gets further reaction with Fe_2O_3; the final sintering reaction is then

$$LiFeO_2 + 2Fe_2O_3 \rightarrow 2Li_{0.5}Fe_{2.5}O_4. \quad (2)$$

In vacuum, any magnetite formed is unoxidized on cooling and there is a decomposition of the lithium ferrite produced in Eq. (2) of the form

$$Li_{0.5}Fe_{2.5}O_4 \rightarrow (1-x)Li_{0.5}Fe_{2.5}O_4 + \frac{5x}{6}Fe_3O_4 + \frac{x}{4}Li_2O\uparrow + \frac{5x}{24}O_2\uparrow. \quad (3)$$

When the specimen is cooled in an atmosphere of oxygen, the final solid product from Eq. (3) is given by the reoxidization reaction

$$(1-x)Li_{0.5}Fe_{2.5}O_4 + \frac{5x}{6}Fe_3O_4 + \frac{5x}{24}O_2 \rightarrow (1-x)Li_{0.5}Fe_{2.5}O_4 + \frac{5x}{4}(\alpha - Fe_2O_3). \quad (4)$$

Therefore, at temperatures in excess of 1000 °C, there is an irreversible loss of lithium and oxygen from the ferrite which is not reversed on cooling in oxygen. In 1970, Ridgley *et al.* investigated the effects of sintering temperature and cooling

rate on the magnetic and crystallographic properties of lithium ferrite.[30] Under 1-atm O_2, lithium ferrite loses oxygen and lithium oxide in increasing amounts with increasing temperature above about 950 °C to 1000 °C. Slow cooling and annealing at a lower temperature bring about reoxidation and precipitation of α-Fe_2O_3. Rapid cooling from the sintering temperature produces anomalously high magnetic moments and lattice parameters; lower temperature annealing and very slow cooling rates produce anomalously low moments. Pointon *et al.* and Ridgley *et al.* almost had the same point of view on lithium and oxygen losses.

2. M-type barium ferrite

Barium ferrite with the chemical formula $BaFe_{12}O_{19}$ (BaM) is widely applied in the fields of permanent magnets, magnetic recording media, and millimeter wave devices due to its high coercively, high saturation magnetization, and low loss in high frequency.[31–37] BaM has a magnetoplumbite structure, with space group $P6_3/mmc$. The magnetic structure of M-type barium ferrite consists of five layers, each of which has one of five distinct Fe crystallographic site in the structure, three octahedral (12k, $4f_2$, and 2a) sites, one tetrahedral ($4f_1$) site and one trigonal bipyramid (2b) site. In addition, it is well known that the Fe^{3+} ions distributed on 12k, 2a, and 2b sites have an up-spin electron configuration, while those located on $4f_1$ and $4f_2$ are spin down. Furthermore, the Fe^{3+} ions on different sites play different roles in the magnetic properties.[38] The magnetic properties of BaM can, therefore, be tailored by substituting other ions for Fe^{3+}.

A wide range of possible compositions of these ferrites have been synthesized by various preparation techniques and different substitutions.[39,40] As cation substitutions is one of the ways to modify the properties of BaM in order to meet the requirements of the specific uses, researchers have modified and improved the properties of M-type ferrites by replacing Ba^{2+} by Sr^{2+}/La^{3+}/Pb^{2+} ions[41,42] or substituting Fe^{3+} ions by trivalent ions like Al^{3+}, Ga^{3+}, Mn^{3+}[35,36] or with the coupled substitution of divalent cations (Zn^{2+}, Co^{2+}, Mg^{2+}, Zr^{2+}, etc) and tetravalent cations (Ti^{4+}, Sn^{4+}, Ir^{4+}, etc).[43–45] In all such modified ferrites, it is necessary that substituted ions maintain electrical neutrality and also have ionic radii close to that of the original one.[45] The extensive work carried out on the synthesis and characterization of M-type barium ferrites is exemplified by $BaFe_{12}O_{19}$, $BaMe_xFe_{12-x}O_{19}$ (Me^{3+} = Al, Cr, Bi, Sc), $BaZn_xSn_xFe_{12-2x}O_{19}$, $BaCo_xRu_xFe_{12-2x}O_{19}$, $BaMe_xIr_xFe_{12-2x}O_{19}$ (Me^{2+} = Co, Zn), $BaMe_xTi_xFe_{11.6-2x}O_{19}$ (Me^{2+} = Co, Zn), and $BaMe_xTi_xFe_{12-2x}O_{19}$ (Me^{2+} = Co, Zn, Mn). Tehrani *et al.*[46,47] reported.

Based on the theory of substitution on M-type barium ferrite materials, we will discuss some substitution projects. First, aluminum has been added with an amount of a divalent ion to give the compounds $BaAl_xFe_{12-x}O_{19}$ using sodium citrate (SC) as the chelating agent by a chemical process.[48] Figures 2 and 3 show that in TGA/DTA and XRD analysis that the crystallization and formation of single phase BaM is completed before 860 °C. The XRD data also confirm Al substituting into Fe sites. The particle size and morphology are not affected by Al doping. Al substitution plays an important role in the magnetic properties. The saturation magnetization (M_s) of $BaAl_xFe_{12-x}O_{19}$ decreases from 51.43 emu/g for the sample with $x = 0$ to 28.32 emu/g at $x = 1.5$. However, the anisotropy field (H_a) increases from 16.21 kOe (1 Oe=79.5775 A/m) to 25.01 KOe. In addition, Ms increases with enhancing the ratio of SC/Ba^{2+} (molar ratio), reaching a maximum when SC/Ba^{2+} is 13.

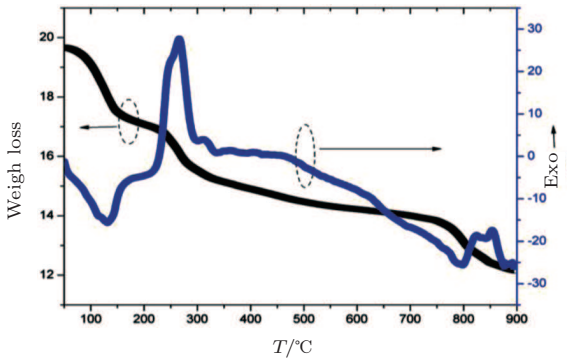


Fig. 2. TGA/DTA curves of as-burnt $BaFe_{12}O_{19}$.

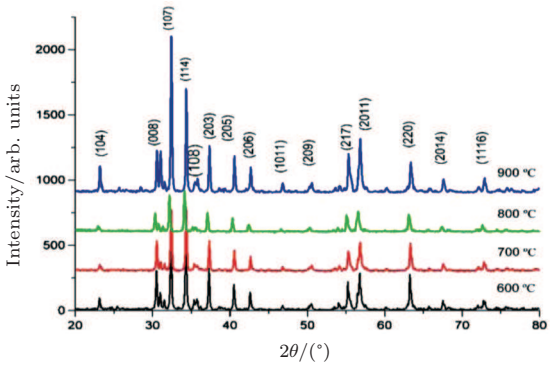


Fig. 3. XRD of $BaFe_{12}O_{19}$ obtained at various sintered temperatures.

Second, M-type barium ferrites with the rare element La has also been reported as yielding excellent properties.[49] The influences of La^{3+} on the structures and magnetic properties of barium ferrites ($Ba_{1-x}La_xFe_{12}O_{19}$) are investigated. Single-phase M-type barium ferrites with chemical composition of $Ba_{1-x}La_xFe_{12}O_{19}$ are formed by sintering at 1100 °C–1175 °C in air. As we can see from Fig. 4, with the value of x increasing, the saturation magnetization (M_s) increases, reaches a maximum at $x = 0.2$ and then decreases, and the coercivity of the sample increases continuously. The value of M_s reaches

a maximum value of 62.8 emu/g at $x = 0.2$ and 1175 °C, and the H_c reaches a maximum value of 3911.5 Oe at $x = 0.6$ and 1125 °C.

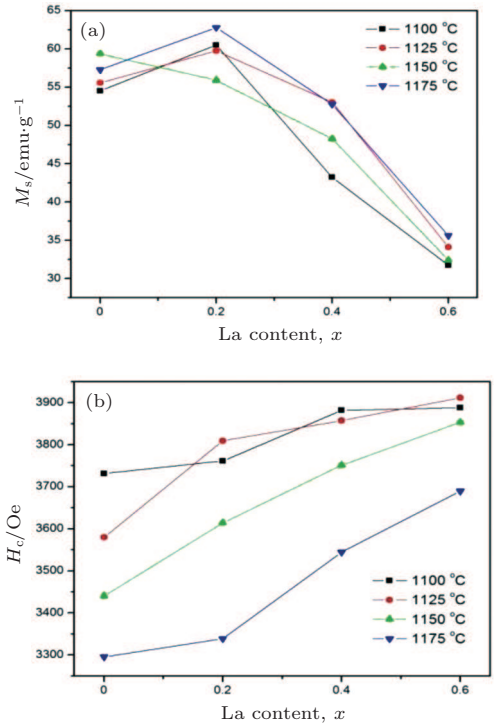


Fig. 4. Variation of M_s (a) and H_c (b) with different sintering temperatures in La-doped samples.

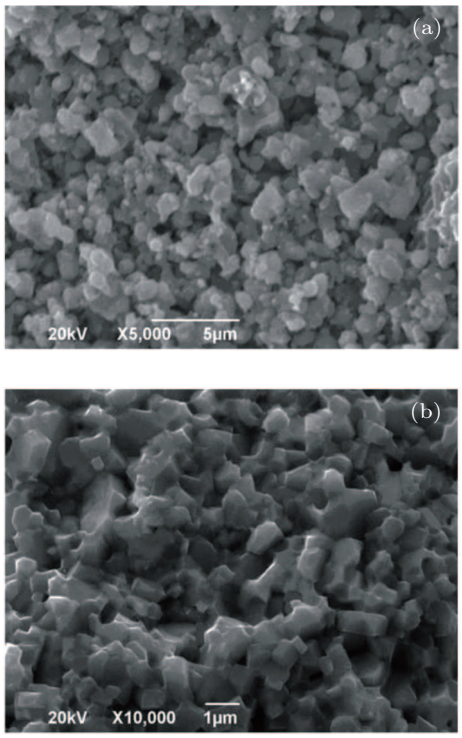


Fig. 5. SEM image of (a) 1150 °C sintered sample without glass additive and (b) 900 °C sintered sample with 5 wt% glass additive.

Third, in order to adapt the development of low temperature co-fired ferrites technology and produce circulators with a multilayer process, the effects of $Zn^{2+}$and Ti^{4+} substitutions on the microstructure and properties of low temperature sintered M-type barium hexaferrites $Ba(ZnTi)_xFe_{12-x}O_{19}$ have been reported.[50] It is found that some Zn^{2+} ions can enter the 2b sublattice, and the saturation magnetization of the samples decrease when x increases. Figure 5 shows that the samples have excellent crystalline grains with a uniform size of about 1.0 μm. A high density of 4.85 g/cm^3 is obtained in the samples sintered at 900 °C with 5 wt% glass additive. The saturation magnetization reaches 63.5 emu/g (about 308 kA/m) and increases as the sintering temperature rises, as in Fig. 6.

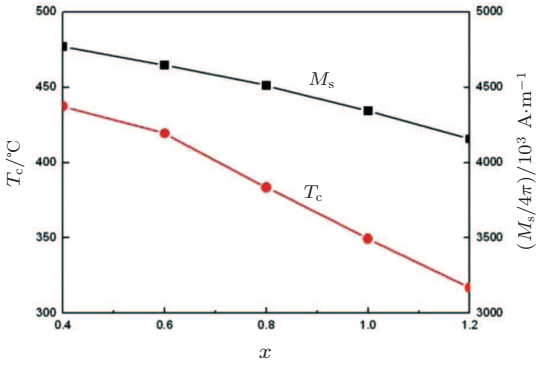


Fig. 6. The dependence of M_s and T_c on the substitution amount.

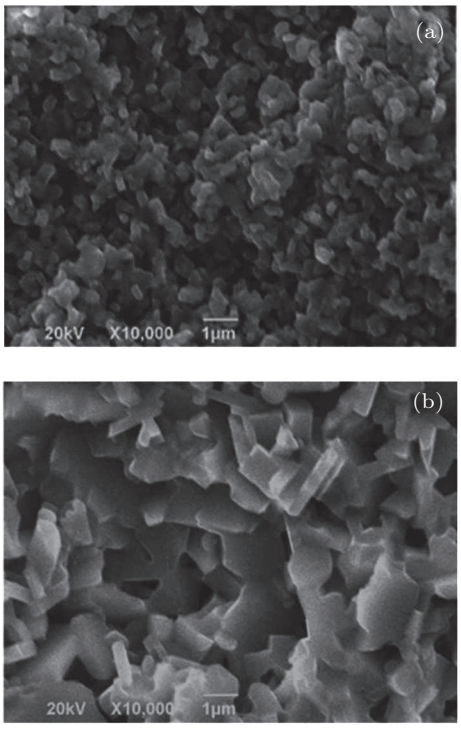


Fig. 7. SEM images of (a) the sample with 3.0 wt% Bi_2O_3 added at the secondary milling with $x = 0$ and (b) the sample with $x = 0.15$.

Lastly, the effects of Co^{2+}, Ti^{4+}, and Bi^{3+} substitution on the microstructures and properties of low temperature fired M-type barium hexaferrites have been studied.[51] Bi^{3+} ions can enter into the 2a sublattice and consequently enhance the

grain growth and densification due to the activation of the lattice. The substitution of Bi^{3+} ions is beneficial to forming the M phase and lowers the sintering temperature to about 900 °C. Figure 7 shows that the samples have excellent crystalline grains with a uniform size of about 1 μm–2 μm. Figure 8 shows that Co^{2+} and Ti^{4+} could adjust the value of coercivity (H_c) and saturation magnetization (M_s). Moreover, nonmagnetic Ti^{4+} ions prefer to enter the $4f_{VI}$ octahedral sites, giving rise to the weakening of the strong 12k-$4f_{VI}$ super-change path, and thus the isotropic exchange energy approaches the other second-order terms on the magnetic Hamiltonian.

Nowadays, in order to enhance the relevant magnetic and electric properties of M-type barium ferrite, fabricating the composite barium ferrites has become a trend and an important research field. Various additives have been added in barium ferrites to meet various practical demands, by sputter deposition, ball milling, evaporation and chemical methods. In general, two main types of materials are used to composite with BaM: the organic and inorganic materials. The organic material and ferrite composites, or inorganic material and ferrite composites, with organized structures usually provide a new functional hybrid, with synergetic or complementary behavior.

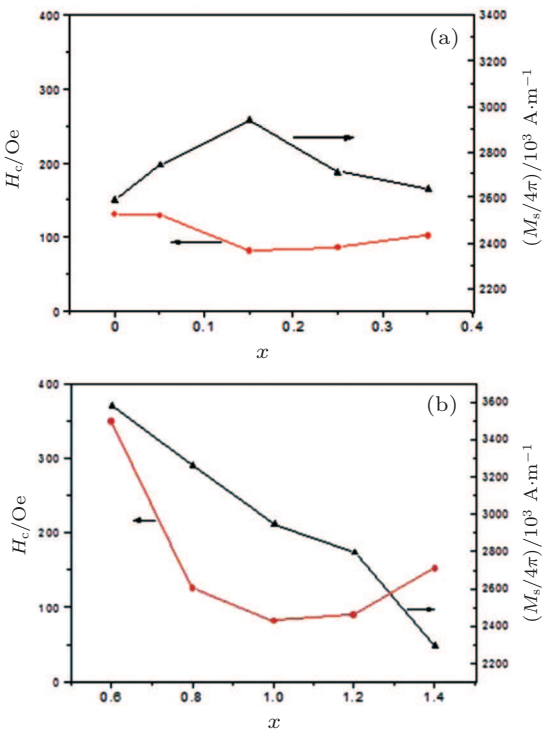


Fig. 8. The dependence of M_s and H_c on the Bi substitution ($y = 1.0$) (a), and on the Co–Ti substitution ($x = 0.15$) (b).

The organic material and BaM hexaferrite composites have been widely and mainly investigated as microwave-absorbing materials. For example, conducting polymers have been used to composite with BaM hexaferrite in order to fabricate the absorbing materials with both excellent electric and magnetic absorbing properties. Polyaniline (PANI) has been studied extensively in recent years because of its ease of synthesis and environmental stability. Ting *et al.* (see Fig. 9) synthesized the PANI/Ba hexaferrite composites by an *in situ* polymerization method, and results showed that the composites exhibit good absorption performance over a broad-band range in the radar band (2 GHz–40 GHz) with good electromagnetic properties.[52] Xu *et al.* successfully synthesized PANI/ferrite nanocomposites with novel coralloid structures (as seen see Fig. 10).[53] Besides, BaM hexaferrites composited with epoxy resin and rubber have also been studied.[54,55]

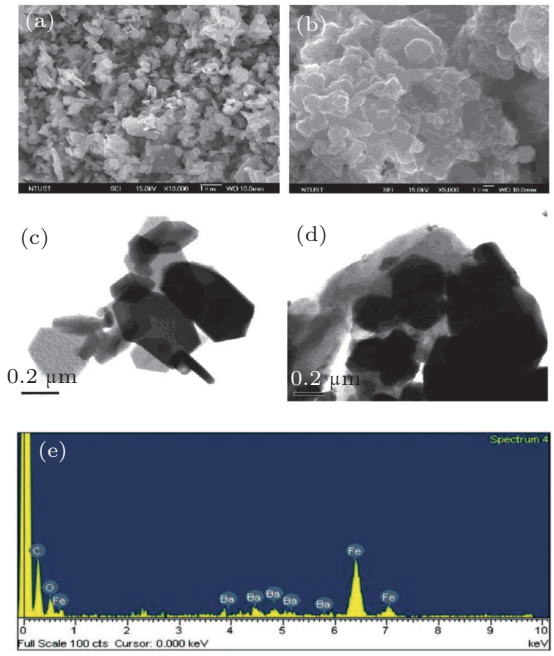


Fig. 9. SEM photographs of (a) Ba ferrite, (b) PANI/Ba ferrite; TEM photographs of (c) Ba ferrite, (d) PANI/Ba ferrite, and (e) EDX spectrum of the PANI/Ba ferrite. (Adapted from Ref. [52].)

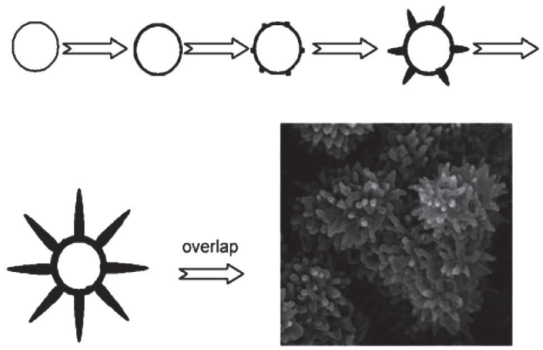


Fig. 10. Schematic of the nucleation and growth of PANI nanofibers with ferrite nanoparticles as nucleation sites and the formation of coralloid nanostructures.[53]

On the other hand, the inorganic material and barium ferrite composites, for both bulks and thin films, have also received considerable attention, especially in the field of magneto-electric composites and hard/soft exchange spring magnet. Compared to metallic systems, composites of spinel

soft ferrite and hard ferrite are promising for advanced permanent magnetic materials, because of their low cost, excellent corrosion resistance, and high electrical resistivity. As for the multiferroic composite, Srinivas *et al.* reported for the first time room temperature multiferroism and magnetoelectric coupling in a $BaTiO_3$–$BaFe_{12}O_{19}$ composite system prepared by solid state sintering, and the magnetoelectric output obtained for the composition 75BT–25BF (wt%) showed a maximum value of 1.45 mV/cm.[56] Films with alternating layers of BaM and barium strontium titanate (BSTO) have been also investigated (see Fig. 11).[57]

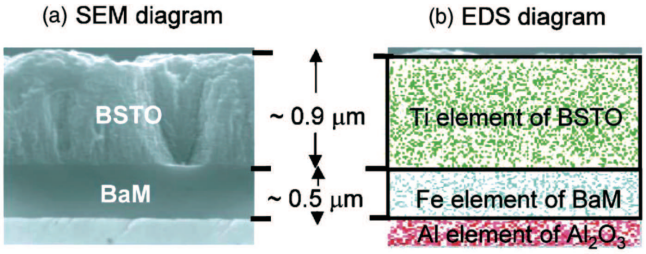


Fig. 11. (a) SEM of the 0.5-μm thick BaM and the 0.9-μm thick BSTO layered structure. (b) Element specific EDS results for the same film.[57]

At the same time, there are two main trends for BaM hexaferrite composites. For one thing, the nanoscale BaM composites are stimulating a sharply increasing number of research activities for their significant technological promise in the novel multifunctional devices. For the other, lowering the sintering temperature of BaM composites to adapt to low-temperature co-fired ceramic (LTCC) technology has become a trend and an important research field.

Due to their excellent properties, barium ferrites have been applied in electronic components, magnetic memories and recording media for several decades. Figure 12 shows all the practical applications of barium ferrite material in recently years. In recent years, the requirements for miniaturization, integration and excellent high-frequency characteristics of microwave devices promote the development of LTCC ferrite materials. The low-temperature sintered ferrites are usually characterized by uniform microstructure, densification and low loss, all of which are beneficial for the properties of high-frequency devices. Lowering the sintering temperature of barium ferrite to adapt to LTCC technology has become a trend and an important research field.

BaM is often used to make a plastic-ferrite as it is a good elastic or plastic binder, and it is easily workable and can be cut into any shape, is familiar to all of us as fridge magnets, both on and inside the door. Magnetic materials for good permanent magnets need to be hard magnetically, and resistant to demagnetization. Therefore, they need to have stable domains, and must have a large remanence and coercivity. A large, square loop with a high energy product is also preferable, so more energy is needed to demagnetize the material. The M-type barium ferrites are ideally suited to such applications.

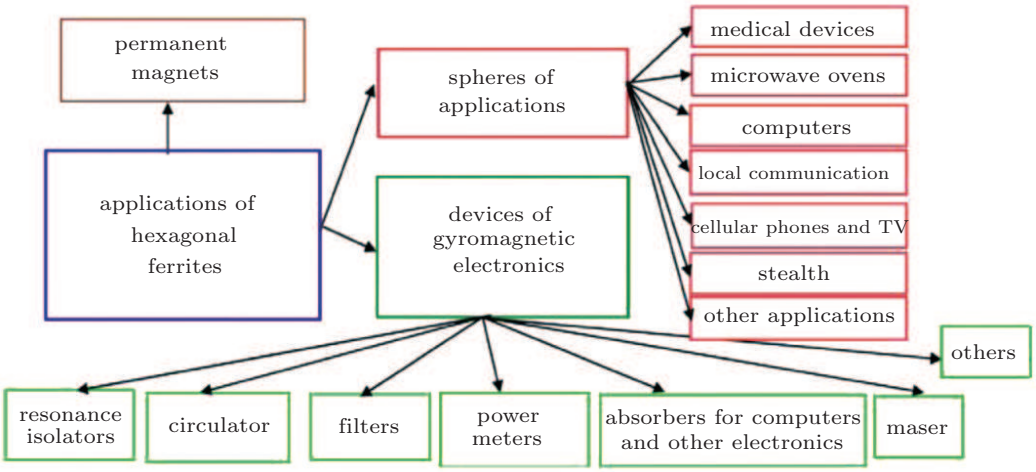


Fig. 12. Practical applications of barium ferrites.

Communication operating frequencies are moving higher, from MW to millimeter waves, requiring the use of hexagonal ferrites. The interest for applications of hexagonal ferrites is between 1 GHz and 110 GHz. Various regions within each band are reserved for radar, mobile, wireless and fixed telecoms, satellites, GPS, and radiolocation, broadcasting, space research and astronomy. Some of the most important barium ferrite millimeter wave (MW) applications are as non-reciprocal devices such as antennas, circulators and isolators, which enable the use of one component to transmit and receive. They effectively switch between transmitting and receiving, magnetostatic MW devices such as delay lines, filters, resonators, and non-linear devices.

In order to minimize the high frequency energy losses, ferrites should have high electrical resistivity. Most hexagonal ferrites have high resistance, leading to very low eddy current

losses, so they are well suited for high frequency applications. Another energy loss called FMR is the main loss in ferrites, so the major goal is to gain narrow FMR line widths. A recent trend in microwave technology is the integration of ferrite devices with semiconductor devices onto a chip. So reducing device volume and weight becomes another research direction.

Information is stored as either 0 or 1 in digital memories, so a square loop with a big remanence is required to ensure the data remains stored and is not lost accidentally, and a high signal to noise ratio is needed. Barium ferrites have this property and can also be cut, stamped, and shaped in a highly mass productive and therefore cheap process, complex shapes are possible with a high degree of dimensional precision. These include flexible sheets, very long or thin shapes, and radial oriented materials, and many electrical components are manufactured in this way.

The large amount of devices operating at MW frequencies in our environment, such as radar and wireless and mobile communications, results in a great increase in EM interference. So there is a growing requirement for MW absorbing materials to reduce interference, shield equipment, shield rooms and chambers for EM compatibility (EMC) testing, and to minimize the harmful effects of EM waves on biological tissues. Barium ferrites are used as microwave absorbers for they can absorb the MW energy around the frequency at which FMR occurs. They are already used as EM absorbers to shield rooms and chambers used for EMC testing of new products and devices at MW frequencies. The EM properties of Barium ferrite composites can be effectively tuned by varying the volume fractions of the constituent phases.

M-type barium ferrites can also find medical applications, for example as components in nuclear magnetic resonance imaging and magnetomotive biomedical implants, but the toxicity of some of the component elements, particularly barium, limits their use in applications where they must be inserted into the human body as particles or fluids.

3. NiCuZn ferrite

Low-temperature-fired NiCuZn ferrites have been widely used in inductive multilayer devices because of their relatively high resistivity and good magnetic properties in the high frequency range.[61,62] Previous investigations of the NiCuZn ferrites were mainly focused on three issues. (i) How to lower the sintering temperature of the NiCuZn ferrites by adding sintering aids or changing the preparation process, including research on the ferrite sintering or densification behavior;[63–66] (ii) How to improve electromagnetic properties such as the resistivity, permeability, and Q-factor of the ferrites, including research on microstructural improvement;[67–71] and (iii) The co-fired characteristics of NiCuZn ferrites with an Ag electrode or other ceramics fired at low temperature.[72–74] Recently, with the development of multilayer technology, ferrites fired at low temperature have been used for power applications such as multilayer power inductors and transformers. However, few studies have investigated the power characteristics of the NiCuZn ferrites fired at low temperature. Therefore, in this section, we analyzed the influence of Co_2O_3 addition on the initial permeability, saturation magnetization, and power loss characteristics of NiCuZn ferrites fired at low temperature.

Table 1. Composition and additions of the samples.

No.	Composition of the samples	Additives and their amounts (wt%)	
		Bi_2O_3	Co_2O_3
No.1	$Ni_{0.35}Cu_{0.2}Zn_{0.45}Fe_{1.96}O_4$	1.5	0
No.2		1.5	0.1
No.3		1.5	0.2
No.4		1.5	0.3
No.5		1.5	0.4

NiCuZn ferrite samples with the composition $Ni_{0.35}Cu_{0.2}Zn_{0.45}Fe_{1.96}O_4$ were prepared by the conventional ceramic processing as previous description. The calcination temperature was chosen as 800 °C. Then, the additives shown in Table 1 were added to the calcined powders. Bi_2O_3 was used as sintering aid and Co_2O_3 was used to improve the power loss characteristics of the ferrite samples. The green product was finally sintered at 900 °C and held for 4h in air, then left to cool inside the electric furnace to room temperature, with heating and cooling rate at 2 °C /min. The density of sintered samples was calculated as the mass/volume ratio. Micrographs were taken using a scanning electron microscope. The initial permeability was measured using a precision LCR meter (Agilent 4284A) at the frequency of 10 kHz. The core loss was measured using a B–H analyzer at room temperature. The saturation magnetization and hysteresis loop were measured using a vibrating sample magnetometer at room temperature.

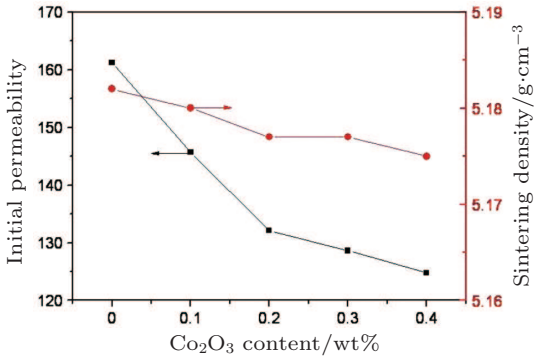


Fig. 13. Variations of initial permeability and sintering density with Co_2O_3 concentration.

Figure 13 shows the initial permeability and sintering density of the samples. The initial permeability continuously

decreases with Co_2O_3 content increasing. The sintering density also decreases with Co_2O_3 content increasing. However, to a lesser extent. Therefore, the obvious decrease in initial permeability cannot be attributed to the slight decrease in sintering density. To identify the factors affecting this phenomenon, we first investigate the microstructure of the samples.

Figure 14 shows representative micrographs of samples without and with the maximum Co_2O_3 content. Both have almost the same average grain size (which is around 5 μm) and grain size distribution. Thus, the decrease in initial permeability cannot be attributed to extrinsic factors such as the grain size and sintering density. It is known that domain wall motion and domain rotation contribute to the initial permeability. The contribution of the latter is negligible at low frequency except when the grain size is so small that only a monodomain state exists.[75] The initial permeability as a function of domain wall motion can be expressed as

$$\mu_i^w = 1 + \frac{3M_s^2 D}{16\gamma_w},$$

where M_s is the saturation magnetization, D is the average grain size, and γ_w is the domain wall energy. Figure 14 shows that all samples had almost the same average grain size, so the dependence of μ_i^w on D can be excluded. Figure 15 shows the saturation hysteresis loop of the samples.

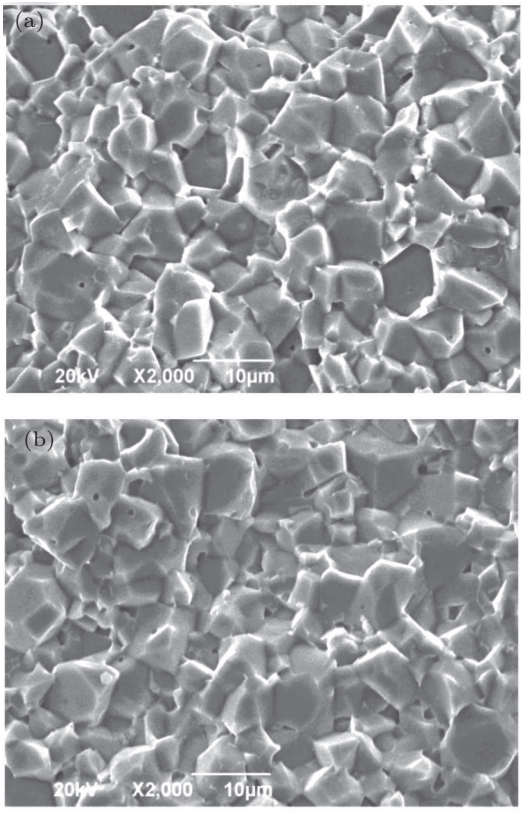


Fig. 14. Micrographs of the samples without (a) and with (b) the maximum Co_2O_3 concentration.

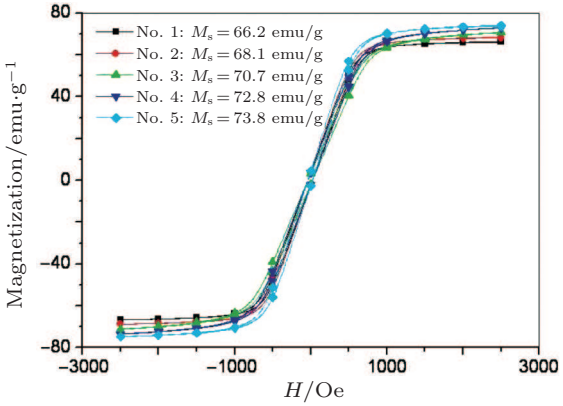


Fig. 15. Saturation hysteresis loop of the samples at 25 °C.

It is evident that the saturation magnetization slightly increased with the Co_2O_3 content, mainly because Co ions prefer to occupy octahedral sites and have a higher magnetic moment than Ni and Cu ions. On the contrary, the increase in saturation magnetization favors an increase in initial permeability. Therefore, the decrease in initial permeability with increasing Co_2O_3 content can be attributed to an increase in domain wall energy. It is known that γ_w is an increasing function of the magnetocrystalline anisotropy (K_1).[75] Cobalt ferrite has a much larger K_1 than that of Ni and Cu ferrites. Furthermore, the concentration of cation vacancies in ferrite samples increases with Co content increasing and therefore the local anisotropy induced by these cation vacancies also increases.[75] Thus, γ_w increases with the Co_2O_3 content and the negative influence of this increase in γ_w is greater than the positive influence of the increase in M_s. As a result, the initial permeability gradually decreases with Co_2O_3 content increasing.

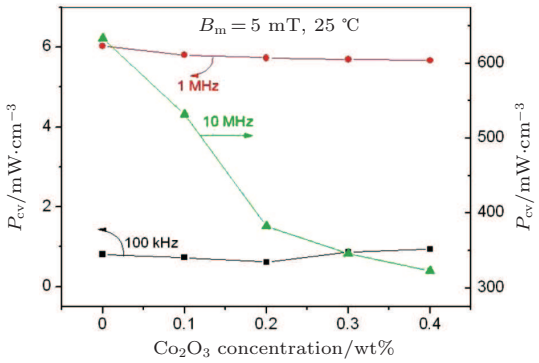


Fig. 16. Frequency dependence of power loss under the flux density of B_m = 5 mT (25 °C).

Table 2. Frequency dependence of power loss under the flux density of B_m = 5 mT (25 °C).

Frequency	P_{cv}/mW·cm^{-3}				
	No.1	No.2	No.3	No.4	No.5
100 kHz	0.81	0.73	0.61	0.87	0.94
1 MHz	6.03	5.80	5.73	5.69	5.67
10 MHz	633.61	531.80	382.62	345.66	322.75

Figure 16 and Table 2 show the frequency dependence of power loss for the samples, P_{cv} increases with the frequency for all the samples. At low frequency, power loss first decreases, and then gradually increases with the increase of Co_2O_3 content. Sample No. 3, which contained 0.2 wt% Co_2O_3, exhibits the lowest power loss. However, when the excitation frequency is increased to 1 MHz and 10 MHz, P_{cv} gradually decreases with increasing Co_2O_3 content. This is particularly evident at 10 MHz. It is known that power loss can be divided into P_h, P_e, and P_r.[58,59,76] At low frequency (100 kHz), P_h is the predominant factor in P_{cv} and is inversely proportional to the cube of the initial permeability.[60] Thus, the decrease in initial permeability with increasing Co_2O_3 content has a negative effect on the power loss. On the other hand, Co ions at B sites can induce local uniaxial anisotropy under the influence of a local Weiss field or under an external field, which favors domain wall "freezing" and a decrease in P_h. This positive influence is more predominant than the negative influence of permeability on P_{cv} for Co_2O_3 content of ≤ 0.2 wt%. With a further increase in Co_2O_3 content, the initial permeability constantly decreases; furthermore, the sintering density also decreases due to the appearance of pores. As a result, the power loss gradually increases. At relatively high frequency, such as 1 MHz or 10 MHz, $P_e + P_r$ increases more obviously than P_h with frequency and becomes the predominant factor in P_{cv}, especially at 10 MHz. Because Co^{2+} has a greater ionization energy (34 eV) than Fe^{2+} (30.6 eV), the Co^{3+} available on Co_2O_3 addition can decrease the Fe^{2+} concentration in ferrite samples according to

$$Fe^{2+} + Co^{3+} \rightarrow Fe^{3+} + Co^{2+}$$

and thus can eliminate the n-type conduction.[77] This favors a decrease in P_e and P_r, leading to a decrease in P_{cv} at high frequency.

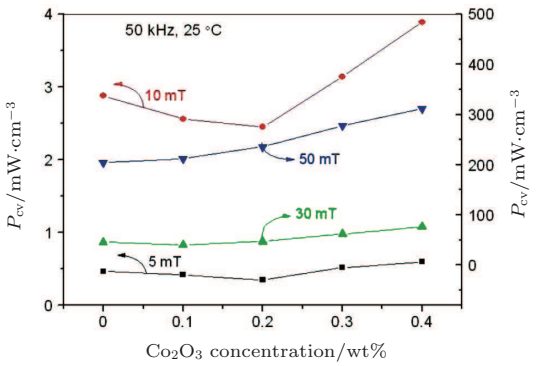


Fig. 17. B_m dependence of power loss at the frequency of 50 kHz (25 °C).

Figure 17 and Table 3 show the variation in power loss with magnetic flux density at a frequency of 50 kHz. At relatively low flux density, P_{cv} first decreases, and then gradually increases with the Co_2O_3 content. This is similar to the trend in Table 3 at low frequency. However, at high flux density, P_{cv} continuously increases with the Co_2O_3 content. According to a previous study, P_h is the predominant factor in P_{cv} at low frequency, and the local uniaxial anisotropy induced by Co_2O_3 addition can "freeze" domain walls and decrease the sample P_h. However, the effect of domain walls "freezing" disappears when the flux density exceeds a critical value, leading to an increase in P_h and P_{cv}. It can be concluded that from Table 3 the critical induction value is 50 mT. If the induction flux density is less than 50 mT, suitable Co_2O_3 addition is useful in decreasing the power loss. However, for an induction flux density greater than or equal to 50 mT, it is better not to add Co_2O_3 when aiming to decrease the power loss of NiCuZn ferrites fired at low temperature.

Table 3. B_m dependence of power loss at the frequency of 50 kHz (25 °C).

B_m	P_{cv}/mW·cm^{-3}				
	No. 1	No. 2	No. 3	No. 4	No. 5
5 mT	0.47	0.42	0.35	0.52	0.60
10 mT	2.88	2.56	2.45	3.14	3.89
30 mT	45.94	40.52	47.54	62.31	76.55
50 mT	203.84	212.41	235.62	277.5	311.86

In summary, the initial permeability gradually decreased with Co_2O_3 content increasing, which was mainly attributed to the influence of local anisotropy induced by Co ions. The saturation magnetization increased with the Co_2O_3 content, which was attributed to the preference of Co ions for octahedral sites and their magnetic moment being higher than that of Ni and Cu ions. Under excitation at low flux density and low frequency, a suitable Co_2O_3 content was useful to decrease P_{cv} because Co ions could "freeze" the domain walls and decrease the sample P_h. When the excitation frequency increased to 1 or 10 MHz, P_{cv} gradually decreased with increasing Co_2O_3 content, because Co^{3+} could decrease the Fe^{2+} concentration and $P_e + P_r$ of the ferrite samples. At low frequency, the effect of domain wall "freezing" by Co ions gradually disappeared with increasing flux density. For a flux density greater than or equal to the critical value of 50 mT, it was better not to add Co_2O_3 when aiming to decrease the power loss of NiCuZn ferrites fired at low temperature.

4. YIG ferrite films and their applications

YIG,Bi:YIG and Bi:LuBiIG garnet films have been chosen in our experiment based on the consideration of propagating loss in the microwave and optical bands. The nonmagnetic GGG (111) substrate was used because of its good match to garnet film in both lattice constant (12.383 Å) and thermal expansion coefficient (9.2×10^{-6}/°C). The mixture of the garnet constituent oxides and the Bi_2O_3 flux were melted

in a platinum crucible at 1000 °C–1050 °C for 24 h, and the solution was homogenized by stirring with a platinum paddle for another 12 h at 1000 °C, and then the temperature was decreased to the growth temperature. The substrate was mounted on a platinum holder with a little slant angle to the liquid surface. During the growth, the substrate was rotated at a rate of 60 rpm–100 rpm, and the rotation direction was reversed after some time. The growth rate of the film can be controlled by the growth temperature and the rotation speed. After growth the substrate was raised from the melt, and rotated at a large speed to spin off the residual flux droplets. And then the substrate was withdrawn from the furnace slowly to avoid cracking due to the surface shrinking (thermal expansion). At last, the film was cleaned in a hot nitric acid to eliminate the Bi_2O_3 flux. A typical growth condition applied in our experiments is listed in Table 4. Note that the furnace temperature profile in the grown zone is strictly controlled, varying less than 0.1°C, and a rotation that changes direction every 3 s during the growth is used in order to get a uniform film. The growth rate of the film is calculated from growth temperature and rotation speed to be 0.417 μm/min. The growth time is 20 min thus a thickness of about 8.34 μm on each side of the GGG substrate is expected for our epitaxial $Bi_{2.1}Lu_{0.9}Fe_5O_{12}$ thin film.

Table 4. Typical parameters for LPE growth process.

Flux composition	Growth temperature	Rotation speed in growth process	Interval of rotation reversal	Rotation after growth
$Bi_{2.1}Lu_{0.9}Fe_5O_{12}$	803 °C	60 rpm	3 s	190 rpm

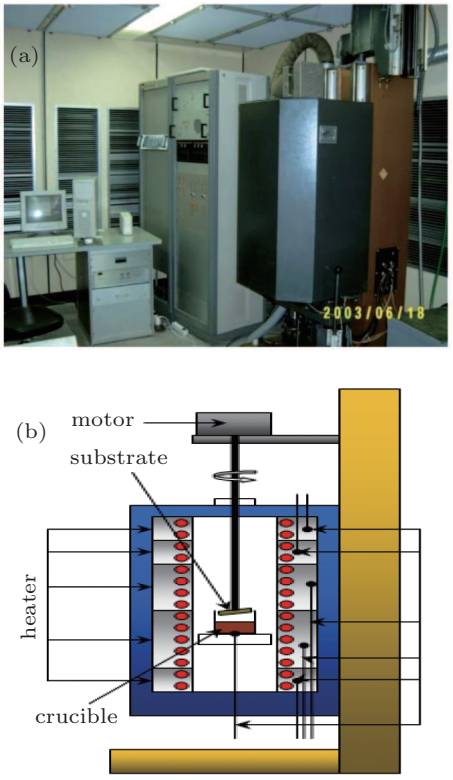


Fig. 18. Growth equipment for garnet LPE microwave crystal. (a) Experimental installation and (b) experimental principle.

The surface morphology of the films was examined by scanning electron microscope (SEM) DS-130C (Akashi, Japan) and by SEIKO SPA-300HV atomic force microscopy (AFM). Absorbance in the optical range was measured by spectrometer, while loss in the microwave range, indicated as ferromagnetic resonance line-width (FMR), was measured by the local excitation of resonance absorption method (or magnetic hole method). The THz response of the films was characteristic of a THz-TDS system (made by Zomeoa Company), the magnetic domain was observed also by scanning electron microscope (SEM) DS-130C (Akashi, Japan). The Faraday rotation effect was measured by magneto-optical (MO) Faraday-effect historiography. The garnet LPE microwave crystal growth equipment used in our experiment is shown in Fig. 18.

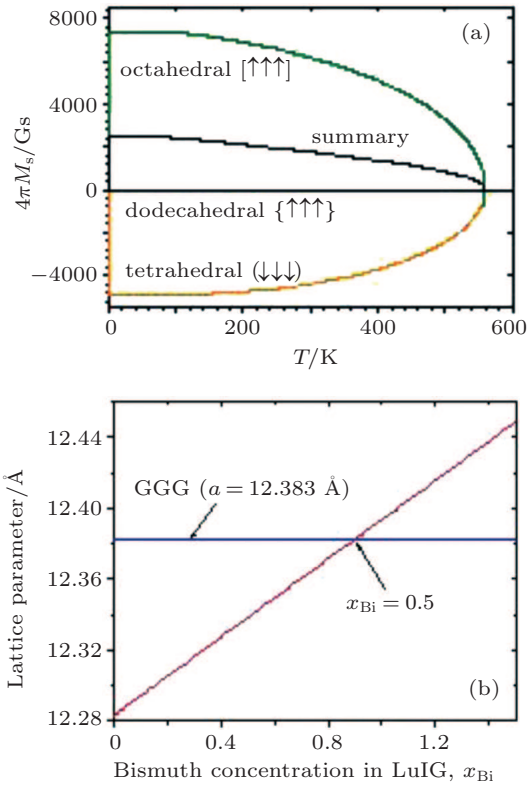


Fig. 19. Lattice parameters as a function of the addition of Bi^{3+} ions. (a) Contribution of different lattice sites to the net magnetic moment of garnet, (b) change of lattice parameter with the doping level of Bi^{3+} ion.

Lead free flux technology of the LPE process was: (i)

Determination of film composition, because net magnetic moment comes only from the contribution of the Fe^{3+} ion, and the Farady effect is related to the energy band width of excited Fe^{3+}. The addition of Bi^{3+} increases the energy band width of excited Fe^{3+}. Evidently, the doping amount of Bi^{3+} ion is very important to increase the Farady angle. (ii) Contra lattice mismatch: The addition of Bi^{3+} ions in garnet film influences the lattice constant of the substrate GGG and needs to be bigger. There are two ways to fit the lattice match, one is growth doping Mg:GGG substrate, the other is LPE Bi:LuIG film, and the good concentration of the Bi ion is about 0.9 at%. The garnet formula $Lu_{2.1}Bi_{0.9}Fe_5O_{12}$ is shown in Fig. 19. (iii) Improvement of growth technique: In common methods, the main fluxes used for iron garnet LPE are $PbO–B_2O_3$, Bi_2O_3, $Bi_2O_3–B_2O_3$, $PbO–Bi_2O_3$, $PbO–Bi_2O_3–B_2O_3$ materials. If we use PbO in the iron garnet LPE process, toxic Pb can deteriorate the film quality, and increase both FMR (ΔH) and the optical absorption coefficient.[78,79] On other hand, doping Bi_2O_3 in garnet film by the LPE method, would increase melt viscosity due to the low fusion point of Bi_2O_3, resulting in a large amount of droplets, due to different precipitation solution rates. So a new buffer LPE method that does not use PbO has been given in this work, it can change a large amount of droplets on the liquid surface into a mirror-like liquid surface before the LPE process finishes, simultaneously control the *c*-axis orientation and growth rate, and get a lower off-axis angle. With it, we can reduce surface defects, reduce loss and increase the Faraday angle in garnet film growth. This is shown in Figs. 20 and 21 .

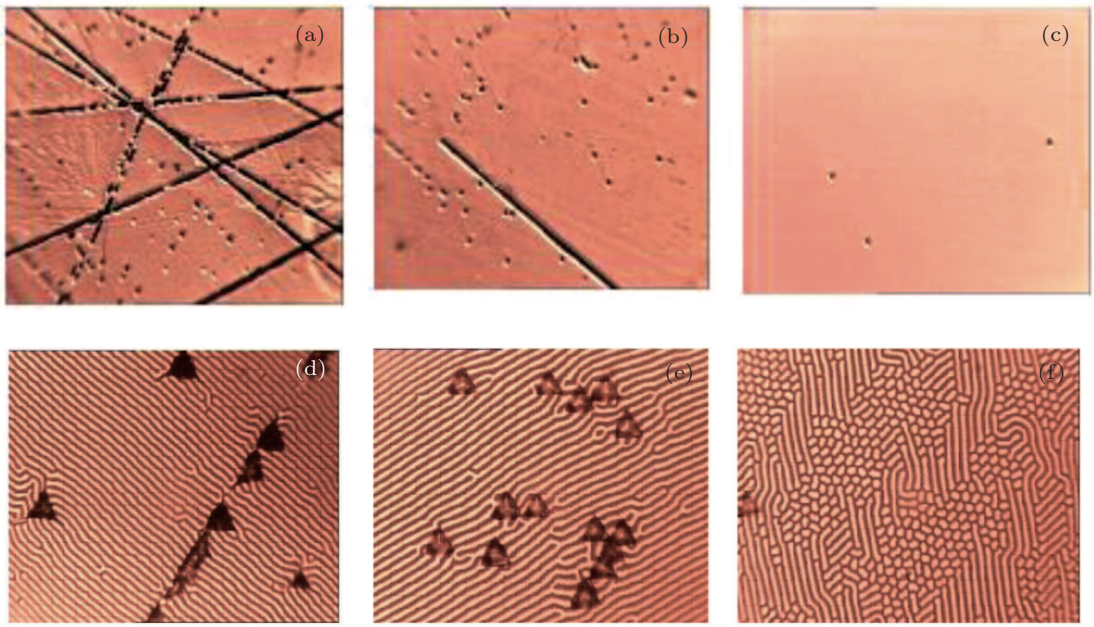


Fig. 20. *c* axis orientation and magnetic domain: (a) off-axis 0.22°, (b) off-axis 0.18°, (c) off-axis 0.14°, (d) off-axis 0.10°, (e) off-axis 0.06°, and (f) off-axis 0.02°.

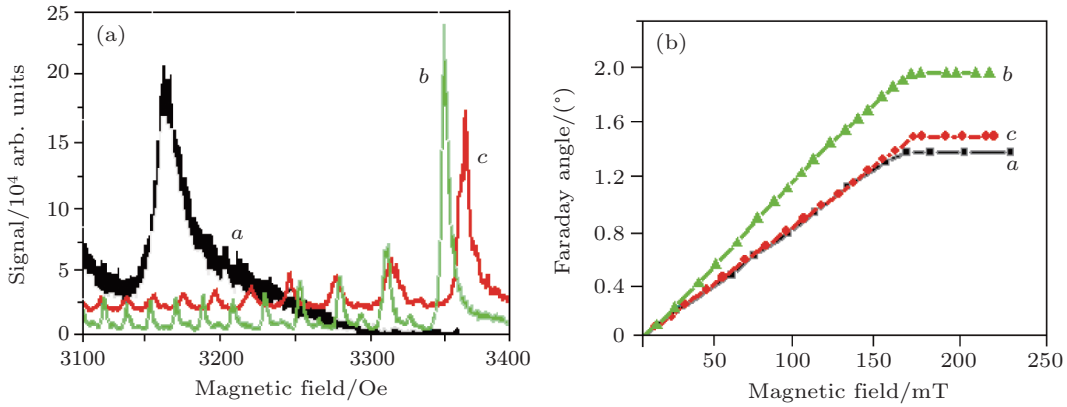


Fig. 21. Off-axis angle (a) and Farady angle (b) vary with the magnetic field.

Shown in Figs. 22 and 23, higher growth rate, we can get an excellent garnet film. With smooth dense surface, lower defect density, higher susceptibility, and smaller FMR. The optimal parameters for Y_3 (Fe, Sc)$_5O_{12}$ films, growth rate$>$ 0.8 μm/min and off-axis angle$<$ 15, for Bi:LuIG film, growth rate$>$ 0.4 μm/min and off-axis angle$<$ 22″.

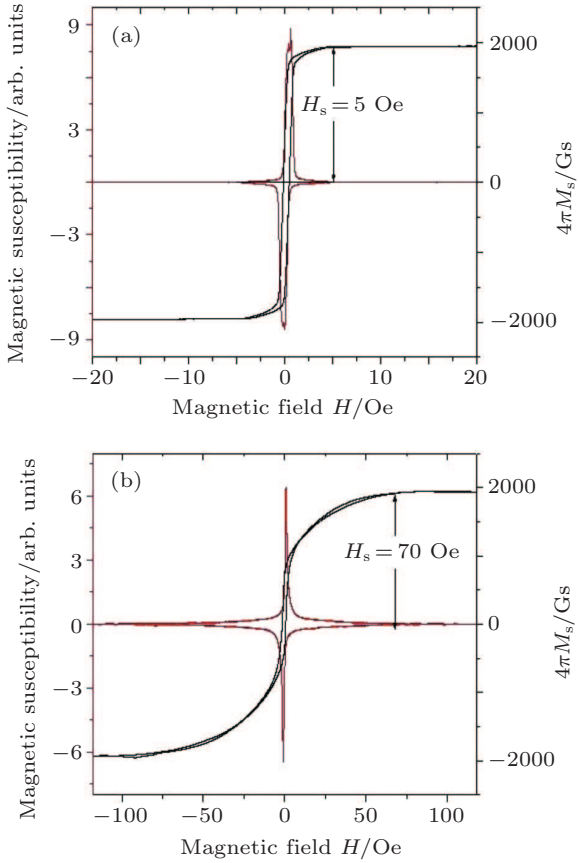


Fig. 22. Magnetic susceptibility and film surface in different growth rates: (a) growth race 0.37 μm/min and (b) growth race 0.85 μm/min.

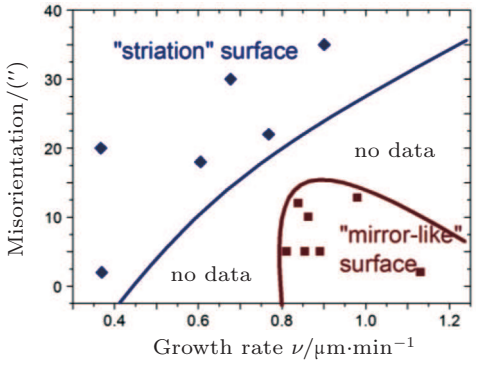


Fig. 23. Function of misorientation as growth rate.

Film fabricated by the new buffer LPE method is clean and flat on the surface, and no micro-cracks and residual flux droplets were observed. Shown in Fig. 24, the surface roughness is also very small, RMS equals to 3.35 nm.

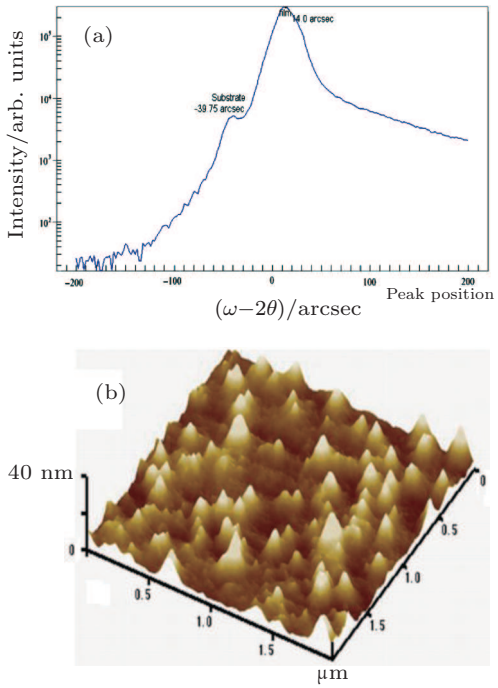


Fig. 24. (a) X-ray diffraction (111)-oriented garnet film on (111) GGG and (b) microstructure of sample.

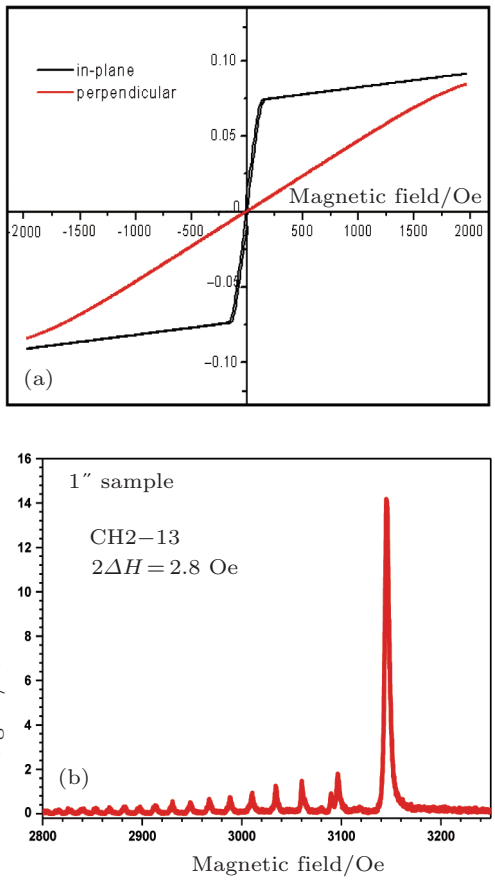


Fig. 25. Magnetic and microwave properties. (a) Magnetic hysteresis loop of sample and (b) FMR spectra of the LuBiIG film on GGG substrate.

The film's magnetic and microwave properties are shown in Fig. 25. Saturation magnetization ($4\pi M_s$) is 1562 Gs, saturation magnetic field (H_{sat}) is 200 Oe and coercivity (H_c) is 11 Oe. It also obviously shows that the smaller size has a

lower FMR than the big size in the buffer LPE method. Higher growth rate can also obtain the lower FMR. The FMR is between 1.4 Oe and 2.8 Oe.

The magneto-optical properties of garnet films fabricated by a new lead-free flux method are shown in Fig. 26. The Faraday angle $\theta_f > 1.6°/\mu m$, 10 times higher than in the common LPE films, and the absorption coefficient is far lower than common LPE methods can achieve.

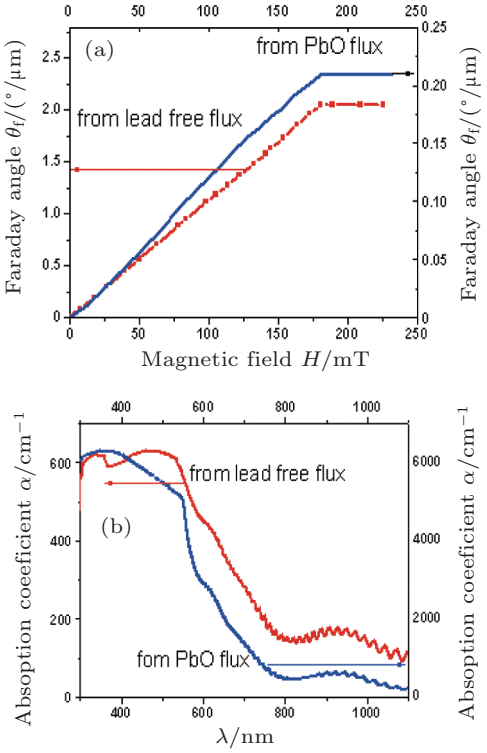


Fig. 26. (a) Faraday angle versus magnetic field and (b) absorption coefficients versus wavelength.

The growth of polycrystalline garnet films by RF magnetron sputtering has been introduced. The effects of substrate, buffer layer, sputtering parameters, and post annealing on the performance of YIG films have been investigated in detail. It has been shown that garnet films with smooth surface and adjustable saturation magnetization can be obtained by using CeO_2 buffer layer. We have also applied the so-called "rapid recurrent thermal annealing" (RRTA) method to control the grain size and distribution of garnet films.

Some applications need polycrystalline garnet films grown on silicon crystal substrates, but garnet/Si is difficult to crystallize and the film has a low density because of boundary and interface defects between two layers.[80,81] Therefore, a buffer layer can be use to improve the properties. In our experiments, the SiO_2 buffer layer and CeO_2 buffer layer were studied; the results show that crystal structure and crystallization rate are obviously improved (See Fig. 27). The saturation magnetization M_s is 25% higher, and coercivity H_c is 10% lower. The main reason is that the Fe^{2+} ion content is reduced about 7.6%, and film density is enhanced in Si/SiO_2/YIG thin films, as shown in Fig. 28.

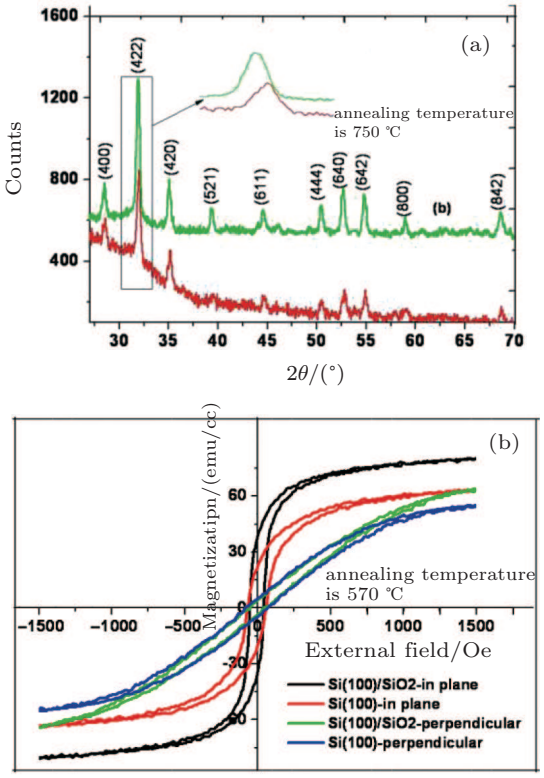


Fig. 27. (a) Structure and (b) magnetic loop trace of garnet film sputtered on SiO_2 buffer layer.

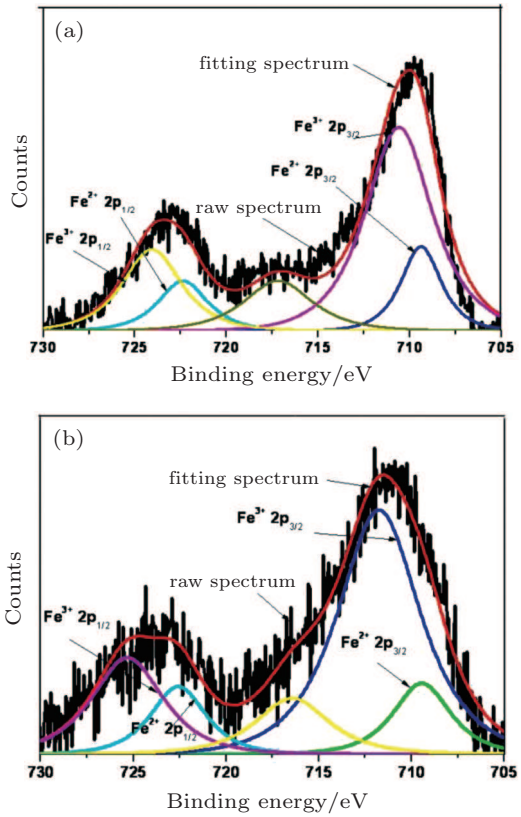


Fig. 28. Fe^{2+} content comparison of silicon substrate with buffer layer. (a) Si/CeO_2/YIG buffer layer and (b) Si/SiO_2/YIG buffer layer.

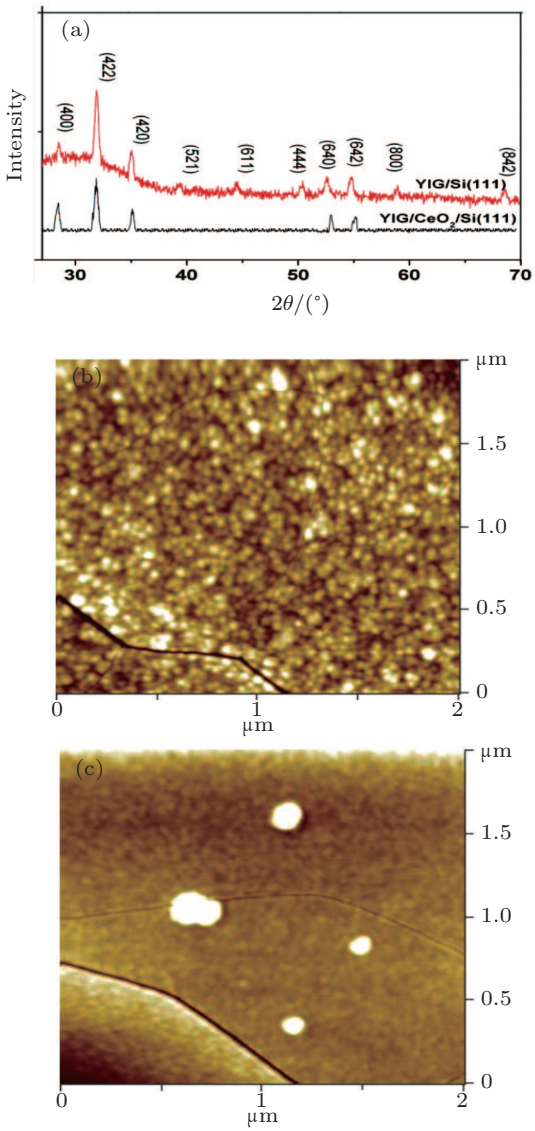


Fig. 29. Comparison of YIG/Si(111) with YIG/ CeO_2/Si(111). (a) X-ray diffraction, (b) SEM of YIG/Si(111), and (c) SEM of YIG/CeO_2/Si(111).

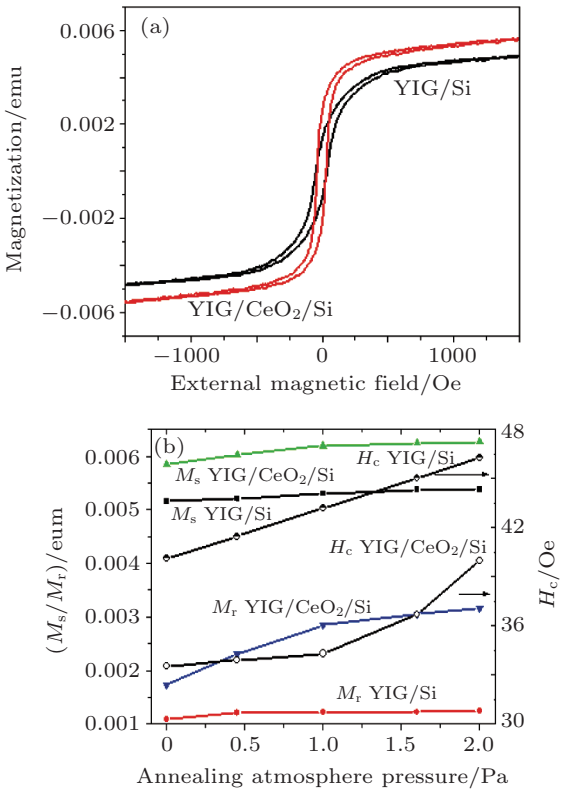


Fig. 30. Magnetic properties of YIG/CeO2/Si(111) films. (a) Magnetic hystersis loop of sample and (b) the value of Ms/Mr of samples.

The CeO_2 buffer layer not only improved crystallization rate and reduced surface roughness, but enhanced M_s about 12%, the M_r about 6%, reduced H_c about 10%, while Fe^{2+} further lowered about 5.2% compared with sputtering on silicon substrate, as shown in Figs. 29 and 30.

In our experiment, the sputtering atmosphere and power are very important parameters to improve the properties of garnet film. The optimum parameters are shown in Table 5.

Table 5. Deposition process parameters.

Composition of target	$Y_3Fe_5O_{12}$
Base pressure of the deposition chamber	2.0×10^{-4} Pa
Temperature of the substrates	500 °C
Sputtering pressure	0.28 Pa
Sputtering atmosphere ratio, $R = O_2/(Ar+O_2)\times100\%$	0%, 2%, 4%
Sputtering power	90 W
Annealing temperature	750 °C
Annealing atmosphere	Vaccum, 0.5 Pa O_2, 1.2 Pa O_2
Heating rate	10 °C/s
Preservation time	10 min

In order to obtain high M_s in YIG/ CeO_2/Si(111) films, growth in pure Ar and annealing in 0.5-Pa oxygen O_2 or growth in Ar+2%O_2 and annealing in vacuum has been assumed. The thin film properties appear in Fig. 31.

The investigation of theories and experiments of magneto-static surface wave (MSSW) filter has been done in this part. The insertion loss model of MSSW filter has been created and the effect of the thickness of garnet film, saturation magnetization and line width to the insertion loss of the filter have been analyzed in detail, as shown in Fig. 32.

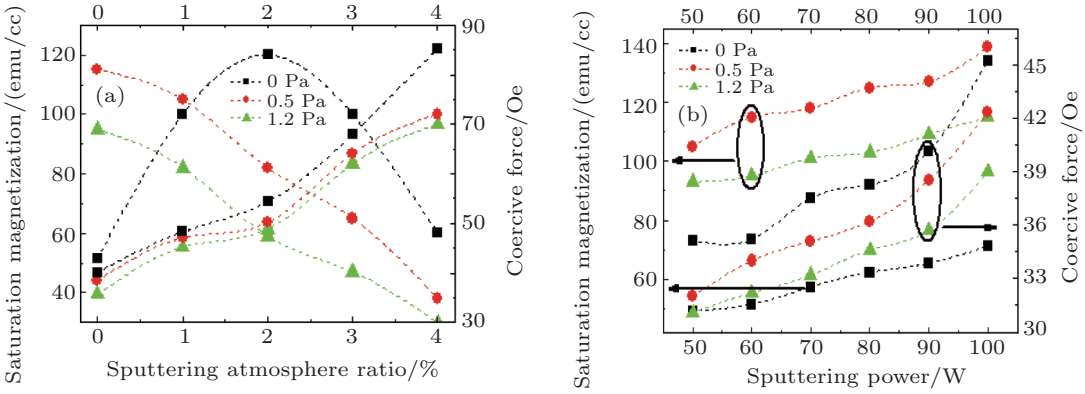


Fig. 31. Saturation magnetization as a function of sputtering atmosphere (a) and power (b).

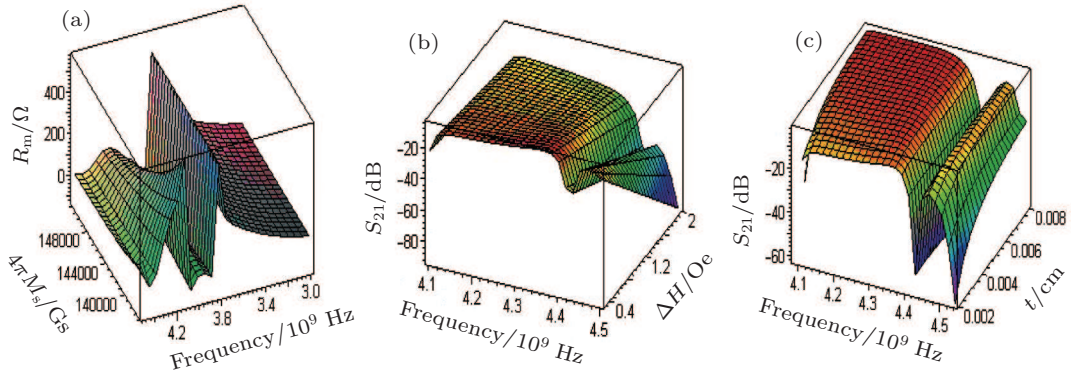


Fig. 32. Properties simulation of the MSSW filter. (a) Frequency dependence of $4\pi M_s$. (b) Frequency dependence of S_{21} and ΔH. (c) Frequency dependence of S_{21} and t.

As shown in Fig. 32, higher saturation magnetization M_s can expand high frequency range application. A sufficient film thickness improves the propagation model and reflection loss, small FMR(ΔH) and low defect density improve the linewidth and the insertion loss.

Meanwhile, the dispersion restraint theory with the double magnetic layer structure has been studied in our work. As shown in Fig. 33, the double magnetic layer structure can effectively suppress the dispersion of the MSSW filter.

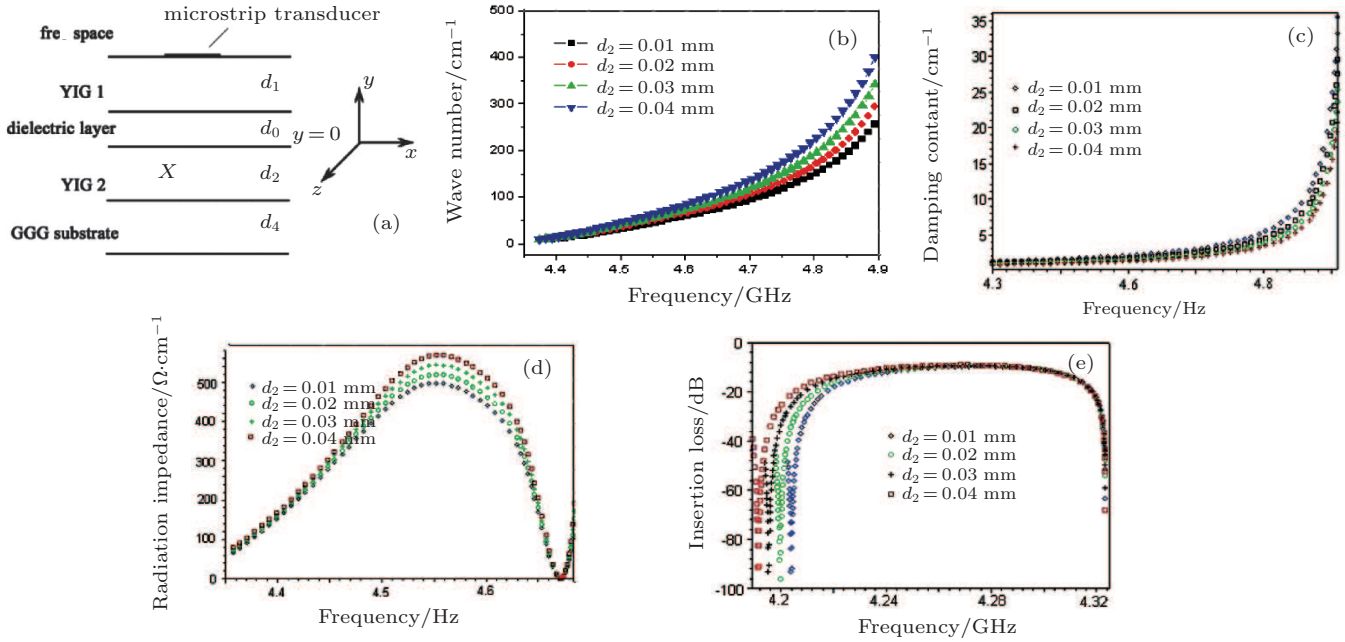


Fig. 33. Double magnetic layer structure (a) and simulation results: (b) frequency dependence of wave number, (c) frequency dependence of damping constant, (d) frequency dependence of radiation impedance, and (e) frequency dependence of insertion loss.

According to theoretical simulation, the MSSW filters with good performance were researched in experiment by using Bi, Lu:YIG film, as shown in Fig. 34.

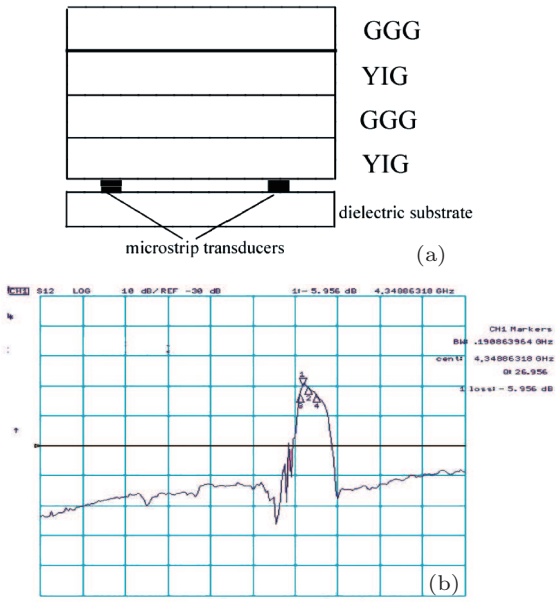


Fig. 34. Comparison of single-layer structure with double magnetic layer structure. (a) The proposed scheme for double magnetic layer structure and (b) magnetic permeability of the MSSW filters.

Comparing measured results of single-layer structure filter and double magnetic layer structure filter, the insertion loss of double magnetic layer structures lowered from 8 dB to 6 dB. The main reason is that magnetic film total thickness increased, the double magnetic layer structure looks like two multiple waveguides, two multiple channels to pass microwaves.

The filter parameters are as follows: the center frequency is between 4.0 GHz and 5.5 GHz, the pass bandwidth is 180±10 MHz, insertion loss is smaller than 8.0 dB (this value can be reduced to 6.0 dB with double magnetic layer structure), and out-band rejection is bigger than 35 dB.

The feasibility investigation of the microwave garnet film circulator has been done. Based on circulator design theory, the effect of substrate thickness or film properties on the circulator performance has been investigated, as shown in Fig. 35.

The results show that the film circulator can be realized from 1.0 GHz to 3.0 GHz by perfecting garnet film preparation technology; however, it still needs a long time to be realized because of its restriction conditions in the high frequency band. When the thickness is lower than 0.3 mm, both standing wave ratio and insertion loss dramatically increase. One efficient way is to increase film thickness and lower the center frequency and reduce the circulator's size.[82–85] Garnet film with thickness $>$ 50 μm (include GGG substrate and thin film$>$ 50 mm) is flexible to design and fabricate a circulator/isolator with the center frequency $<$ 3 GHz.

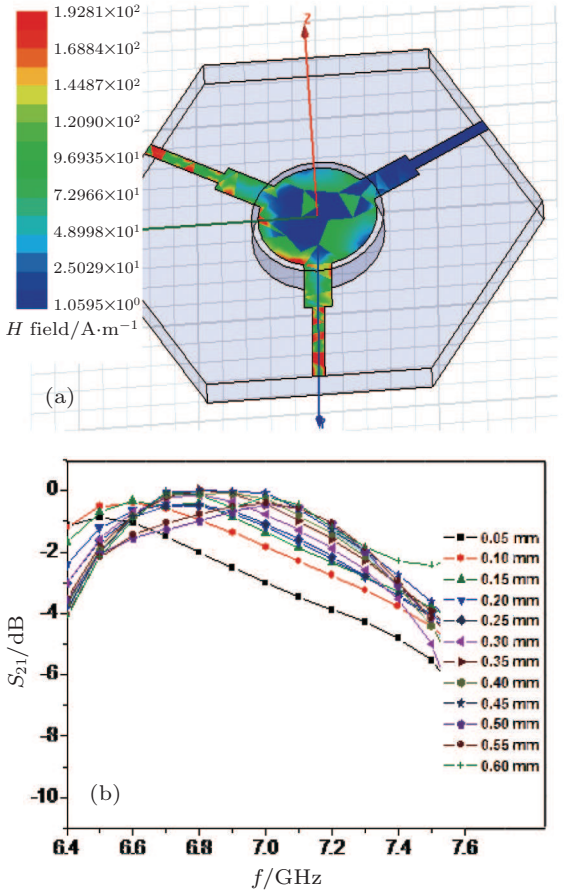


Fig. 35. Simulation results of garnet circulator based on Bi, Lu: YIG film. (a) Structure and magnetic field distribution, (b) the wave absorbing properties with different thickness of films.

5. Lithium ferrite and its applications

In spinel ferrites, the magnetic anisotropy of single-crystal lithium ferrite is strong, which leads to high coercivity and high low-field loss, increasing the energy consumption of microwave devices. In the 1970's and 1980's, American scholars conducted a study on the magnetic anisotropy of lithium ferrites used below the K_u-band frequency that had guidance significance for applications of lithium ferrites at higher frequency bands. In 1974, Argentina *et al.* investigated basic magnetic properties, insertion loss, and power handing capability of lithium ferrites in latching applications at frequencies in the S, C, X, and K_u bands, and compared in these applications with nickel ferrites, magnesium ferrites and garnets.[86] The results showed that low magnetization ($<$ 800 G) lithium–titanium ferrites with the best possible temperature performance have inherently high anisotropy, which is responsible for excessive low field magnetic loss. The method used for reducing anisotropy in the lithium-ferrite system compromises temperature performance but does result in low loss. For a fixed magnetization, power handling capability, and loss, the Gd-YIG's are less temperature sensitive than low anisotropy lithium–titanium ferrites. Lithium ferrites are superior to the nickel ferrites and magnesium fer-

rites used at frequencies in the X band and above. Improvements on the order of 15%–50% in remanence ratio are obtainable with the lithium-ferrite system in comparison with other spinels. In 1982, Patton *et al.* studied the magnetization of Li–Zn ferrite ($Li_{0.5-x/2}Zn_xFe_{2.5-x/2}O_4$) over the temperature range 4 K–950 K and the relations between magnetization and temperature.[87] The results showed that magnetization at 20 kOe and 4 K increases with Zn content and then declines, and a qualitative fit obtained for the J_{AB}/J_{BB} ratio in the range 3–4. The decrease of Curie temperature is linear from $x = 0$ to $x = 0.7$, and then drops sharply to the low values for $x = 0.9$ and 1.0. In the same year, Brower *et al.* studied order-disorder effects in the anisotropy of substituted lithium ferrite.[88] Co- and MnCo-substituted Li ferrite revealed changes in K_1 concurrent with ordering, which are much larger than those occurring in pure Li ferrite. The spin wave line width ΔH_k also exhibited large changes. This was because Co migrates to the tetrahedral (A) sites and low level Mn substitutions modify Co behavior.

In the last ten years, microwave devices have been developed toward miniaturization, low loss, and low cost, which requires the microwave material applied in them to develop in the direction of high frequency, low loss, and low cost. In 2000, Pardavi-Horvath M systematically analyzed the microwave applications of soft ferrites.[89] To reduce porosity and dielectric loss tangent, small amounts of Bi_2O_3 and MnO_2 are added. Inclusion of Co increases the limiting power. Commercial micro-strip circulators (TransTech) for the 6 GHz–18 GHz frequency range are based on LiMnTi spinel ferrites having good thermal stability. The paper stressed that polycrystalline materials could be affected by non-uniform microstructure, magnetic and dielectric loss. Some common defects (pores, grain boundary, holes, other phases, and local stress) can affect the magnetic and dielectric loss by reducing initial permeability and increasing width and coercivity.

Lithium ferrites not only have excellent static magnetic properties and microwave properties, but also have good dielectric properties, in order to adapt to the low-loss and high-performance microwave devices. In the last ten years, Indian scholars have investigated dielectric properties of lithium ferrites and analyzed the effects of frequency and polarization ions on dielectric constant and dielectric loss, finding that controlling the content of Fe^{2+} could adjust dielectric constant and dielectric loss. In 2002, Venudhar *et al.* prepared lithium–cobalt ferrites ($Li_{0.5-0.5x}Co_xFe_{2.5-0.5x}O_4$) by the double sintering technique, the final sintering temperature being 1100 °C.[90] Figure 36 shows the variation of dielectric constant (ε') with frequency at room temperature for Li–Co mixed ferrites. A close examination of the figure indicates that the dispersion of ε with frequency reaches its maximum value in the case of lithium ferrite and the magnitude of dispersion decreases as more and more Co is added, becoming a minimum for the ferrite having 24% of Co.

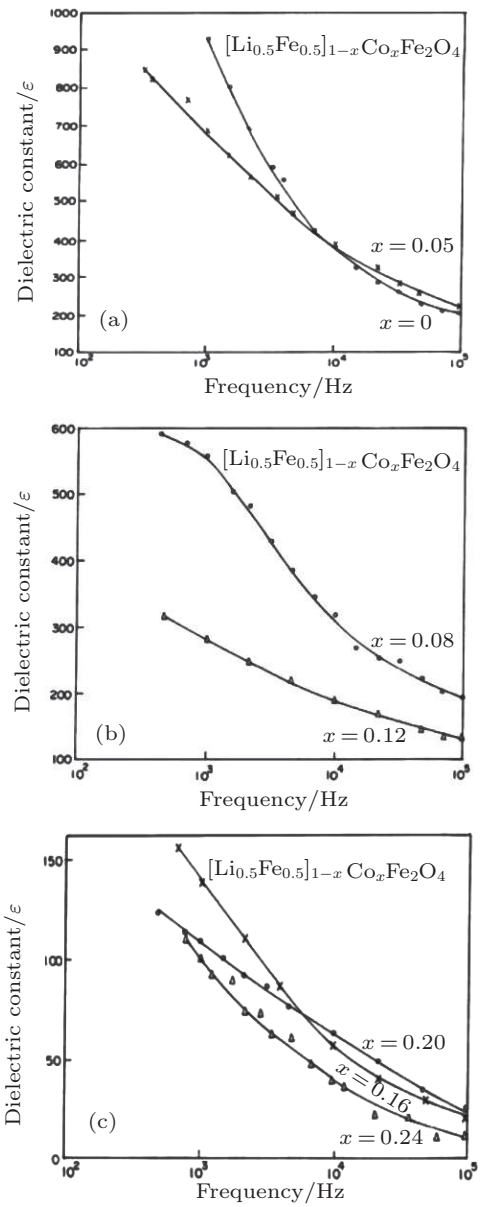


Fig. 36. Variation of dielectric constant with frequency for Li–Co mixed ferrites at room temperature. (a) x=0 and x=0.05, (b) x=0.08 and x=0.12, and (c) x=0.20 and x=0.24.

In 2003, Ravinder *et al.* studied the effects on dielectric properties of lithium ferrites by germanium substitution at low frequencies from 1 MHz to 13 MHz.[91] The dielectric constant and dielectric loss tangent both decrease as the amount of Ge increases but the dielectric loss tangent is abnormal and shows a peak at 10-MHz frequency. In 2007, Gupta *et al.* discussed dielectric and magnetic properties of citrate-route-processed Li–Co spinel ferrites.[92] Figure 37 shows variation of dielectric constant for composition (a) $x = 0.0$, and (b) $x = 0.4$ for $Li_{0.5-x/2}Co_xFe_{2.5-x/2}O_4$ as a function of frequency at different sintering temperatures. Dielectric constant (ε') for $Li_{0.5}Fe_{2.5}O_4$ is greater than that for $Li_{0.3}Co_{0.4}Fe_{2.3}O_4$

and $Li_{0.2}Co_{0.6}Fe_{2.2}O_4$. In the case of $Li_{0.5}Fe_{2.5}O_4$, the number of ferrous ions is maximum value, and hence, it is quite possible for these ions to polarize to the maximum extent. The dielectric constant (ε') is observed to decrease with cobalt content up to composition $x = 0.4$ and then further found to increase with increasing cobalt content. The lowest value of ε' for composition $x = 0.4$ is observed to be 11.2.

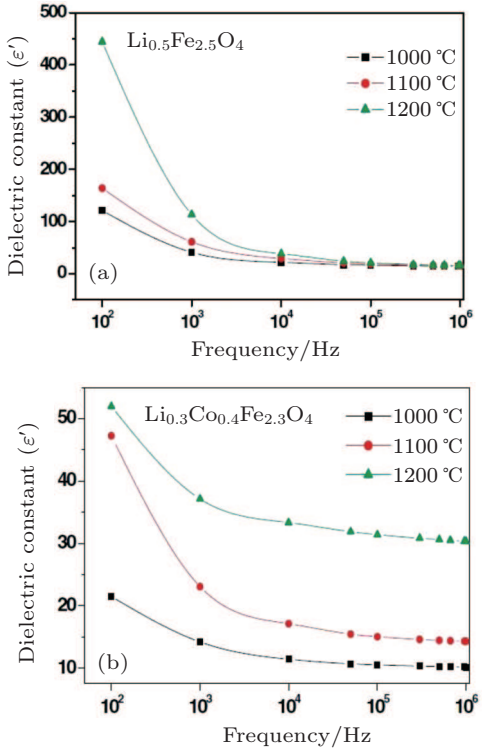


Fig. 37. Variation of dielectric constant for composition (a) $x = 0.0$, and (b) $x = 0.4$ for $Li_{0.5-x/2}Co_xFe_{2.5-x/2}O_4$ as a function of frequency at different sintering temperatures.

In the same year, Verma *et al.* analyzed the influence of silicon substitution on the properties of lithium ferrite.[93] The article pointed out: increasing amount of silicon substitution could promote grain growth. The dielectric constant and loss tangent of mixed Li–Si ferrite both decrease with increasing silicon concentration in the ferrite. Such variations in dielectric properties are due to Fe^{2+} and Fe^{3+} concentrations on octahedral sites and electronic hopping frequency between Fe^{2+} and Fe^{3+} ions. In 2009, Verma *et al.* studied remarkable influence on the dielectric and magnetic properties of lithium ferrite ($Li_{0.5}Zn_xTi_xMn_{0.05}Fe_{2.45-2x}O_4$, $x = 0.00$–0.30) by Ti and Zn substitution.[94] The results indicate that with Ti and Zn concentration increasing in the ferrite, the dielectric constant significantly increases, the dielectric loss tangent decreases and ac resistivity and dc resistivity both increase slightly.

In the past, bulk lithium ferrite materials were typically investigated by conventional oxide ceramic processes, which was due to the maturity of this technology, its simple equipment and the low cost of raw materials. However, there are some disadvantages: high temperatures make the single-phase structure of ferrite materials difficult to control, resulting in poor consistency between batches and difficulty in device integration for LTCF (low temperature co-fired ferrite) technology. To further reduce the sintering temperature, a great many scholars embarked on studies of nano-ferrites and thin films to the requirements of IC integrated design for chip-based components. However, the performance of thin film materials is far from the requirements of applications, and it is difficult to meet the material requirements of phased array radar microwave phase shifters in the short term. High surface activity of ferrite nanopowders can help achieve low-temperature sintering. The production methods of ferrite production are self-propagating high-temperature synthesis, the sol–gel method and the high energy mechanical milling method. In 1999, Cho *et al.* prepared two ferrimagnetic oxides, $Y_2Gd_1Fe_5O_{12}$ and $Li_{0.3}Zn_{0.4}Fe_{2.3}O_4$ using conventional solid state reaction, and then modified by the sol–gel particulate coating process utilizing additives of MnO_2 and SiO_2, and investigated in conjunction with grain growth kinetics and grain boundaries.[95] Interestingly, the addition of small amounts of MnO_2 and SiO_2 using the sol–gel coating process led to different results for the two magnetic materials. In the case of $Y_2Gd_1Fe_5O_{12}$, the additives inhibited grain growth because Si-rich precipitates were segregated along the grain boundary and exerted a drag force against grain boundary movement. On the other hand, the same additives acted as an accelerator for grain growth by forming a glassy phase at the grain boundaries for $Li_{0.3}Zn_{0.4}Fe_{2.3}O_4$. These results were correlated to observed structural characteristics of the materials. In 2002, Gee *et al.* synthesized nano-sized $(Li_{0.5x}Fe_{0.5x}Zn_{1-x})Fe_2O_4$ ($0 \leq x \leq 1$) particles with high magnetic saturation and low coercivity by energetic ball milling technique.[96] The results are as follows: the ball milled, partially crystallized lithium zinc ferrite starts to crystallize at about 600 °C.

The lithium zinc ferrite particle size was in the range of 20 nm to 50 nm. Regardless of the annealing temperature, the saturation magnetization increases with x increasing and reaches the maximum (about 80 emu/g) at $x = 0.7$, followed by a decrease to 60 emu/g for $x = 1$. On the other hand, the coercivity of $x = 0.7$ composition decreases with increasing annealing temperature. In 2003, Yue *et al.* studied the magnetic properties of titanium-substituted LiZn ferrites via a sol–gel auto-combustion process.[97] The results indicate that the dried gels can burn in a self-propagating combustion process in air to transform into single-phase, nano-crystalline ferrite particles. The low-temperature sintering was realized using the synthesized powders, and the sintered ferrites had fine-grained microstructures and excellent magnetic properties. Appropriate amounts of titanium substituted for Fe in LiZn ferrites could significantly increase the permeability value. The prepared LiZn ferrites were good materials for multilayer chip induc-

tors. In 2008, Soibam *et al.* investigated effects of cobalt substitution on the dielectric properties of Li–Zn ferrites by sol–gel method. The study results are as follows: with the addition of Co^{2+} ions, lattice constant, sintering density, average grain size and resistivity increase, and porosity and dielectric constant decrease.[98] In 2009, Soibam *et al.* also studied Ni substitution on the dielectric properties of Li-Zn ferrites by the citrate precursor method.[99] The study results are as follows: lattice constant and dielectric constant decrease with the increase of Ni substitution; the sample dielectric constant, dielectric loss tangent and electrical conductivity increase with temperature increasing. In the same year, Jiang *et al.* investigated sintering characteristics of LiZn ferrites fabricated by a sol–gel process.[100] The results indicate that when compared with a traditional ceramic process, the sol–gel process could slightly bring down the sintering temperature of LiZn ferrite, whereas the microstructures are not homogeneous in the sintered samples. The sintering mechanisms of LiZn ferrites sintered at 1360 °C were studied, revealing that during sintering, solid mass transfer is dominant in the LiZn ferrites fabricated by a traditional ceramic process, while in the gel-derived ferrites, gas mass transfer is dominant. In 2010, Abdullah Dar *et al.* studied the dielectric properties of nano-sized pure and Al-doped lithium ferrite by the citrate gel auto combustion method.[101] Figures 38(a) and 38(b) show the variation of the real and imaginary parts of the dielectric constant of nano $Li_{0.5}Al_xFe_{2.5-x}O_4$ ($0.0 \leq x \leq 0.4$) ferrite samples with frequency 50 Hz to 5 MHz at room temperature.

It can be observed that all the compositions exhibit dielectric dispersion where both the real and imaginary dielectric constants decrease rapidly with increasing frequency in the low-frequency region, while it approaches almost frequency-independent behavior in the high-frequency region. The decrease in the imaginary part of the dielectric constant is more pronounced than in the real dielectric constant. From Fig. 38(c), it is apparent that dielectric loss shows the peaking nature for all the compositions, and a slight shift in these maxima is observed. It is also noted that the height of the peak decreases with the increase in Al concentration.

Microwave ferrites demand low ferromagnetic resonance line width and low dielectric loss. According to the current application situation, microwave ferrite shifters are in great demand, and they require ferrites with low loss, and a unit length of ferrite ring maintains a sufficient differential phase shift. Thus, the ferrite materials need to have a high gyro-magnetic property (high saturation magnetization) to reduce the volume and insertion loss of ferrite phase shifters. However, in a certain frequency band, high saturation magnetization material is not conducive to improving the high power of shifters. It is necessary to determine suitable saturation magnetization according to the situation of phase shifter load power and saturation magnetization normalization. Ion replacement is a common method adopted to adjust the saturation magnetization of lithium ferrite in different microwave frequency bands.

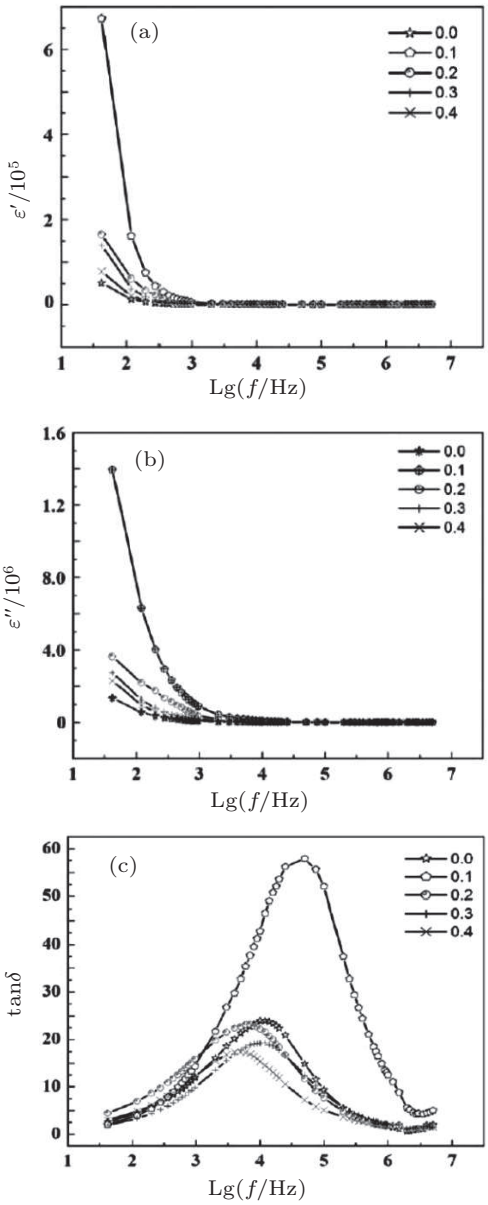


Fig. 38. Variation of (a) real, (b) imaginary part of dielectric constant and (c) loss tangent of $Li_{0.5}Fe_{2.5-x}Al_xO_4$ as a function of frequency.

In terms of X-band, the common substitution is Ti^{4+}, Zn^{2+}, and Al^{3+} ion replacement.[102–104] Non-magnetic Ti^{4+} ion substitution has been found to cause a substantial decline in magnetization, which can be attributed to the molecular magnetic moment decrease caused by Ti^{4+} ions entering octahedral sites sublattice of lithium ferrite. Therefore, Ti^{4+} ion substitution is not conducive to produce high saturation magnetization ferrites. Non-magnetic Zn^{2+} ions easily enter the magnetic moment of tetrahedral sites, which causes the magnetic moment of A site sub-lattice to decrease and the magnetic moment of B site sub-lattice to increase. Then, the molecular magnetic moments of Li ferrite increase,

thereby enhancing the ferrite materials saturation magnetization. However, excessive Zn^{2+} ions substitution can weaken the strength of A–B exchange interaction $Fe^{3+}_{(A)}$–O^{2-}–$Fe^{3+}_{(B)}$, which cause saturation magnetization and Curie temperature to decrease.[105,106] Therefore, adequate Zn^{2+} ions substitution in lithium ferrite, which can be prepared for high gyromagnetic ferrite material, is adopted as the material applied for Ka-band ferrite phase shifter. In addition, Zn^{2+} ions can effectively reduce the ferrite material magnetic anisotropy constant, coercivity and ferromagnetic resonance line width, and Zn^{2+} ions substitution can promote the ferrite material densification and grain growth to a certain extent.[107] LiZn ferrite, which performs a wide range of variable saturation magnetization, high Curie temperature, low stress sensitivity, and low fabrication cost, is apt to be fabricated into microwave/millimeter wave devices, e.g., ferrite phase shifter. Ka-band ferrite phase shifter is a crucial component of phase array radar, and the LiZn ferrite applied in it should have excellent gyro-magnetic property (high saturation magnetization), good soft magnetic property (low coercivity), and a rectangular characteristic (high remanence ratio). Furthermore, low microwave losses (low ferromagnetic resonance line width and dielectric loss) are required to reduce insertion loss. However, LiZn ferrites have the difficulties of densification sintering, which are demanded doping and replacements with other ions or to be sintered at high temperature ($\sim$ 1160 °C). High temperature sintering could improve material density and saturation magnetization, and reduce coercivity. But sintering over 1000 °C, the equilibrium oxygen partial pressure of ferrite surface is larger than atmospheric pressure, which causes the ferrite oxygen decomposition, Li_2O evaporation and Fe^{2+} ions emergence. As a result, the probability of electronic transition between Fe^{2+} and Fe^{3+} increases, dielectric loss significantly increases, and resistivity substantially declines.[108] In order to reduce the effect of Li^{2+} ion volatilization, Teo *et al.* and Zhao *et al.* added a low melting point material (Bi_2O_3) by liquid phase sintering to reduce the sintering temperature to about 1000 °C.[109,110] Meanwhile, Luo *et al.* investigated Li-excess formulation to compensate for Li volatilization and got good results.[111]

To sum up, a great many scholars proposed various ways of improving lithium ferrite materials' magnetic and microwave properties, which laid a good foundation for applying lithium ferrite materials to microwave ferrite devices (such as ferrite phase shifter) at higher frequencies.

6. Conclusions

LTCC technology has played a key role in most device systems and will continue to do so as it provides a unique multilayer structural system and frequency-selective properties. The development and understanding of ferrite materials was one of the successes of physics and chemistry in the 20th century and continuing research is required to provide excellent materials in the millimeter-wave and microwave range. We introduced a novel LTCC ferrite material suitable for microwave and millimeter-wave applications. In all cases, improving properties, lowering the sintering temperature and increasing integration will continue to be required. Only these properties can assure that real multilayer components can be produced.

References

[1] Wise A T, Rocks J, Laughlin D E, Mchenrym M E, Yoon S D, Vittoria C and Harris V G 2011 *J. Appl. Phys.* **109** 07E535
[2] Ounnunkad S, Phanichphant S, Winotai P and Tang I M 2007 *Phys. Stat. Sol. (b)* **244** 2190
[3] Pullar R C 2012 *Prog. Mater. Sci.* **57** 1191
[4] How H, McKnight S W, Oliver S A, Zavracky P M, McGruer N E and Vittoria C 1999 *IEEE Trans. Microwave Theor. Tech.* **47** 1982
[5] Wang K L and Mittleman D M 2004 *Nature* **432** 376
[6] Fisher A D, Lee J N, Gaynor E S and Tveten A B 1982 *Appl. Phys. Lett.* **41** 779
[7] Tsai C S, Young D, Chen W, Adkins L, Lee C C and Glass H 1985 *Appl. Phys. Lett.* **47** 651
[8] Duvillaret L, Garet F and Coutaz J L 2007 *Appl. Opt.* **38** 409
[9] Tien P K, Martin R J, Wolfe R, Le Craw R C and Blank S L 1972 *Appl. Phys. Lett.* **21** 207
[10] Marcelli R, Rossi M and Guglielm M 1992 *IEEE Trans. Magn.* **28** 3303
[11] Chen C L 1989 *IEEE Trans. MTT* **37** 239
[12] EI-Sharawy E B and Guo J S 1995 *IEEE Trans. MTT* **1** 107
[13] Kobljanskyj Y 2002 *IEEE Trans. Magn.* **38** 3102
[14] Adam J 1985 *IEEE Trans. Magn.* **24** 1794
[15] Boudiar T, Payet-Gervy B, Blanc-Mignon M F, Rousseau J J, Berre M L and Joisten H 2004 *J. Magn. Magn. Mater.* **284** 77
[16] Yang Q H, Zhang H W, Liu Y L and Wen Q Y 2007 *IEEE Trans. Magn.* **43** 3652
[17] Zhang H W, Yang Q H and Bai F M 2011 *IEEE Trans. Magn.* **47** 295
[18] Zhang W K and Liu G Q 2004 *J. Appl. Phys.* **95** 1
[19] Hirano T, Hotaka H, Komuro E, Namikawa T and Yamazaki Y 1992 *IEEE Trans. Magn.* **28** 3237
[20] Suzuki T, Sequeda F, Hoa D, Huang T C and Gorman G 1990 *J. Appl. Phys.* **67** 4435
[21] Zhang H W, Kim H J and Yang S Q 1995 *J. Magn. Magn. Mater.* **150** 377
[22] Zhang H W, Kim H J and Yang S Q. 1995 *Mater. Sci. Eng. B* **34** 53
[23] Tsay C Y, Liu K S and Lin I N 2004 *J. Eur. Ceram. Soc.* **24** 1057
[24] Luther L C, Lecraw R C, Dillon J F and Wolfe R 1982 *J. Appl. Phys.* **53** 2478
[25] Thavendrarajah A, Paravi-Horvath M and Wigen P E 1989 *IEEE Trans. Magn.* **25** 4015
[26] Metselaar R and Huyberts M A H 1973 *J. Phys. Chen. Solids* **34** 2257
[27] Zhou X T, Cheng W J, Lin F L, Ma X M and Shi W Z 2006 *Appl. Surf. Sci.* **253** 2108
[28] Dumont Y, Keller N, Popova E, Schmool D S, Tessier M, Bhattacharya S, Stahl B, da Silva R M C and Guyot M 2007 *Phys. Rev. B* **76** 104413
[29] Ridgley D H, Lessoff H and Childress J D 1970 *J. Am. Ceram. Soc.* **53** 304
[30] Argentina G M and Baba P B 1974 *IEEE Trans. Microw. Theory Tech.* **22** 652
[31] Zou H, Li S H, Zhang L Q, Yan S N, Wu H G, Zhang S and Tian M 2011 *J. Magn. Magn. Mater.* **323** 1643
[32] Nie Y, Harward I, Balin K, Beaubien A and Celinski Z 2010 *J. Appl. Phys.* **107** 073903
[33] Dehinger A S, Leberre M, Canut B, Chatelon J P, Albertini D, Perrot S, Givord D and Rousseau J J 2010 *J. Magn. Magn. Mater.* **322** 3293
[34] Morisako A, Matsumoto M and Naoe M 1996 *J. Appl. Phys.* **79** 4881
[35] Harris V G, Chen Z H, Chen Y J, Yoon S and Sakai T 2006 *J. Appl. Phys.* **99** 08M911
[36] Chen Y J, Geiler A L, Chen T Y, Sakai T, Vittoria C and Harris V G 2007 *J. Appl. Phys.* **101** 09M501

[37] Ounnunkad S, Phanichphant S, Winotai P and Tang I M 2007 *Phys. Stat. Sol. (b)* **244** 2190
[38] Xu Y, Yang G L, Chu D P and Zhai H R 1990 *Phys. Stat. Sol. (b)* **157** 685
[39] Zhang X, Duan Y P, Guan H T, Liu S H and Wen B 2007 *J. Magn. Magn. Mater.* **311** 507
[40] Santos J V A, Macedo M A, Cunha F, Sasaki J M and Duque J G S 2003 *Microelectron. J.* **34** 565
[41] Singhal S, Namgyal T, Singh J, Chandra K and Bansal S 2011 *Ceram. Int.* **37** 1833
[42] Onreabroy W, Papato K, Rujijanagul G, Pengpat K and Tunkasiri T 2012 *Ceram. Int.* **38** S415
[43] Mariño-Castellanos P A, Moreno-Borges A C, Orozco-Melgar G, Garcia J A and Govea-Alcaide E 2011 *Physica B* **406** 3130
[44] González-Angeles A, Lipka J, Grusková A, Sláma J, Jančárik V and Slugeň V 2010 *J. Phys.: Conf. Ser.* **217** 012137
[45] Meaz T M and Koch C B 2004 *Hyperfine Interactions* **156–157** 341
[46] Zhao W Y, Zhang Q J, Tang X F and Cheng H B 2005 *Chin. Sci. Bull.* **50** 1404
[47] Tehrani M K, Ghesemi A, Moradi M and Alam R S 2011 *J. Alloy. Compd.* **509** 8398
[48] Chen D M, Liu Y L, Li Y X, Yang K and Zhang H W 2013 *J. Magn. Magn. Mater.* **337–338** 65
[49] Li J, Zhang H W, Li Y X, Li Q and Qin J F 2012 *Acta Phys. Sin.* **61** 227501 (in Chinese)
[50] Liu Y L, Li Y X, Zhang H W, Chen D M and Wen Q Y 2010 *J. Appl. Phys.* **107** 09A507
[51] Jia L J, Zhang H W, Yin S M, Bai F M, Liu B Y, Wen Q Y and Shen J 2011 *J. Appl. Phys.* **109** 07E317
[52] Ting T H and Wu K H 2010 *J. Magn. Magn. Mater.* **322** 2160
[53] Xu P, Han X J, Jiang J J, Wang X H, Li X D and Wen A H 2007 *J. Phys. Chem. C* **111** 12603
[54] Sugimoto S, Kondo S, Okayama K, Nakamura H, Book D, Kagotani T and Homma M 1999 *IEEE Trans. Magn.* **35** 3154
[55] Makled M H, Matsui T, Tsuda H, Mabuchi H, EI-Mansy M K and Morii K 2005 *J. Mater. Process. Tech.* **160** 229
[56] Srinivas A, Gopalan R and Chandrasekaran V 2009 *Solid State Commun.* **149** 367
[57] Das J, Kalinikos B A, Roy B A and Patton C E 2007 *Appl. Phys. Lett.* **91** 172516
[58] Parvatheeswara R B, Ovidiu C, Ioan D and Leonard S C 2006 *J. Magn. Magn. Mater.* **304** E749
[59] Parvatheeswara R B, Kim C O and Kim C 2007 *Mater. Lett.* **61** 1601
[60] Kondo K, Chiba T and Yamada S 2004 *J. Magn. Magn. Mater.* **254–255** 541
[61] Jeong J and Han Y H 2004 *J. Mater. Sci.* **15** 303
[62] Wang H B, Liu J H, Li W F, Wang J B, Wang L, Song L J, Yuan S J and Li F S 2008 *J. Alloy. Compd.* **461** 373
[63] Mürbe J and Töpfer J 2005 *J. Electroceram.* **15** 215
[64] Kin O L and Frank R S 2003 *J. Magn. Magn. Mater.* **256** 221
[65] Ahmed T T, Rahman I Z and Rahman M A 2004 *J. Mater. Proc. Tech.* **153–154** 797
[66] Su H, Zhang H W, Tang X L and Jing Y L 2006 *J. Magn. Magn. Mater.* **302** 278
[67] Mürbe J and Töpfer J 2006 *J. Electroceram.* **16** 199
[68] Krishnaveni T, Kanth B R, Raju V S R and Murthy S R 2006 *J. Alloy. Compd.* **414** 282
[69] Hsu W C, Chen S C, Kuo P C, Lie C T and Tsai W S 2004 *Mater. Sci. Eng. B* **111** 142
[70] Li Y, Zhao J P, Han J C and He X D 2005 *Mater. Res. Bull.* **40** 981
[71] Roy P K and Bera J 2006 *J. Magn. Magn. Mater.* **298** 38
[72] Hong S H, Park J H, Choa Y H and Kim J 2005 *J. Magn. Magn. Mater.* **290–291** 1559
[73] Miao C L, Zhou J, Cui X M, Wang X H, Yue Z X and Li L T 2006 *Mater. Sci. Eng. B* **127** 1
[74] Hsiang H I, Liao W C, Wang Y J and Cheng Y F 2004 *J. Eur. Ceram. Soc.* **24** 2015
[75] Byun T Y, Byeon S C and Hong K S 1999 *IEEE Trans. Magn.* **35** 3445
[76] Rao B P and Caltun O F 2006 *J. Optoelectron. Adv. Mater.* **8** 995
[77] Su H, Zhang H W, Tang X L, Liu B Y and An Y L 2007 *Phys. Stat. Sol. (a)* **204** 576
[78] Dumont Y, Keller N, Popova O, Schmool D S, Gendron F, Tessier M and Guyot M 2004 *J. Magn. Magn. Mater.* **272–276** E869
[79] Dumont Y, Keller N, Popova E, Schmool D S, Bhattacharya S, Stahl B, Tessier M and Guyot M 2005 *J. Appl. Phys.* **97** 10
[80] Park M B and Cho N H 2001 *J. Magn. Magn. Mater.* **231** 253
[81] Kang Y M, Wee S H, Baik S I, Min S G and Yu S C 2005 *J. Appl. Phys.* **97** 10A319
[82] Qin F W, Zhang Q, Bai Y Z, Ju Z H, Li S M, Li Y C, Pang J Q and Bian J M 2012 *Rare Metals* **31** 150
[83] How H, Oliver S A, McKnight S W, Zavracky P M, McGruer N E, Vittoria C and Schmidt R 1998 *IEEE Trans. Microwave Theor. Tech.* **46** 1645
[84] Neidert R E and Philips P M 1993 *IEEE Trans. Microwave Theor. Tech.* **41** 1081
[85] Cheng X B, Wu Y F and Yu Q X 2011 *Rare Metals* **20** 197
[86] Argentina G M and Baba P B 1974 *IEEE Microwave Theor. Tech.* **22** 652
[87] Patton C E, Edmondson C A and Liu Y H 1982 *J. Appl. Phys.* **53** 2431
[88] Brower C J and Patton C E 1982 *IEEE Trans. Magn.* **18** 1619
[89] Martha P H 2000 *J. Magn. Magn. Mater.* **215–216** 171
[90] Venudhar Y C and Mohan K S 2002 *Mater. Lett.* **54** 135
[91] Ravinder D and Reddy A C 2003 *Mater. Lett.* **57** 2855
[92] Gupta N, Kashyap S C and Dube D C 2007 *Phys. Stat. Sol. (a)* **204** 2441
[93] Verma V, Pandey V, Kotnala R K, Kishan H, Kumar N and Kothari P C 2007 *J. Alloy. Compd.* **443** 178
[94] Verma V, Pandey V, Shukla V N, Annapoorni S and Kotnala R K 2009 *Solid State Commun.* **149** 1726
[95] Cho Y S, Hoelzer D T, Burdick V L and Amarakoon V R W 1999 *J. Appl. Phys.* **85** 5220
[96] Gee S H, Hong Y K, Park M H, Erchson W and Lamb P J 2002 *J. Appl. Phys.* **91** 7586
[97] Yue Z X, Zhou J, Wang X H, Gui Z L and Li L T 2003 *J. Eur. Ceram. Soc.* **23** 189
[98] Soibam I, Phanjoubam S, Sharma H B, Sarma H N K, Laishram R and Prakash C 2008 *Solid State Commun.* **148** 399
[99] Soibam I, Phanjoubam S and Prakash C 2009 *J. Magn. Magn. Mater.* **321** 2779
[100] Jiang X N, Lan Z W, Yu Z, Liu P Y, Chen D Z and Liu C Y 2009 *J. Magn. Magn. Mater.* **321** 52
[101] Dar M A, Batoo K M, Verma V, Siddiqui W A and Kotnala R K 2010 *J. Alloy. Compd.* **493** 553
[102] Kuanr B K, Singh P K, Kishan P, Kumar N, Rao S L N, Signh P K and Srivastava G P 1988 *J. Appl. Phys.* **63** 3780
[103] Xu Z C 2003 *J. Appl. Phys.* **93** 4746
[104] Oliver S A, Harris V G, Hamdeh H H and Ho J C 2000 *Appl. Phys. Lett.* **76** 2761
[105] Li C X, Li Z H, Du X Y, Du C L and Liu J B 2012 *Rare Metals* **31** 31
[106] Dooling T A and Cook D C 1991 *J. Appl. Phys.* **69** 5352
[107] Dixon S 1967 *J. Appl. Phys.* **38** 1417
[108] Liu J J, Wang R, Yin H Y, Liu X L, Si P Z and Du J 2012 *Rare Metals* **31** 547
[109] Teo M L S, Kong L B, Li Z W, Lin G Q and Gan Y B 2008 *J. Alloy. Compd.* **459** 557
[110] Zhao X K, Zhang B P, Zhao L, Zhu L F, Li Y and Cheng L Q 2012 *Rare Metals* **31** 590
[111] Luo M, Jiang X N, Yu Z, Sun K, Lan Z W and Wang Z K 2011 *Piezoelect Rocs & Acoustooptics* **33** 608 (in Chinese)